The Astronomical Journal, 160:111 (21pp), 2020 September https://doi.org/10.3847/1538-3881/ab9f2d

KELT-25 b and KELT-26 b: A Hot Jupiter and a Substellar Companion Transiting Young A Stars Observed by TESS*

Romy Rodríguez Martínez[1], B. Scott Gaudi[1], Joseph E. Rodriguez[2], George Zhou[2], Jonathan Labadie-Bartz[3], Samuel N. Quinn[2], Kaloyan Penev[4], Thiam-Guan Tan[5], David W. Latham[2], Leonardo A. Paredes[6], John F. Kielkopf[7], Brett Addison[8], Duncan J. Wright[8], Johanna Teske[9,59], Steve B. Howell[10], David Ciardi[11], Carl Ziegler[12], Keivan G. Stassun[13,14], Marshall C. Johnson[15], Jason D. Eastman[2], Robert J. Siverd[16], Thomas G. Beatty[17], Luke Bouma[18], Timothy Bedding[19], Joshua Pepper[20], Joshua Winn[18], Michael B. Lund[11], Steven Villanueva, Jr.[21,60], Daniel J. Stevens[22,23,61], Eric L. N. Jensen[24], Coleman Kilby[24], Jeffrey D. Crane[9,25], Andrei Tokovinin[26], Mark E. Everett[27], C. G. Tinney[28], Michael Fausnaugh[21], David H. Cohen[24], Daniel Bayliss[29,30], Allyson Bieryla[2], Phillip A. Cargile[2], Karen A. Collins[2], Dennis M. Conti[31], Knicole D. Colón[32], Ivan A. Curtis[33], D. L. Depoy[34,35], Phil Evans[36], Dax L. Feliz[13], Joao Gregorio[37], Jason Rothenberg[38], David J. James[2,39], Michael D. Joner[40], Rudolf B. Kuhn[41,42], Mark Manner[43], Somayeh Khakpash[20], Jennifer L. Marshall[34,35], Kim K. McLeod[44], Matthew T. Penny[45], Phillip A. Reed[46], Howard M. Relles[2], Denise C. Stephens[40], Chris Stockdale[47], Mark Trueblood[48], Pat Trueblood[48], Xinyu Yao[20], Roberto Zambelli[49], Roland Vanderspek[21], Sara Seager[21,50,51], Jon M. Jenkins[10], Todd J. Henry[6], Hodari-Sadiki James[6], Wei-Chun Jao[6], Sharon Xuesong Wang[9], Paul Butler[25], Ian Thompson[9], Stephen Shectman[9], Robert Wittenmyer[8], Brendan P. Bowler[52], Jonathan Horner[8], Stephen R. Kane[53], Matthew W. Mengel[8], Timothy D. Morton[54], Jack Okumura[8], Peter Plavchan[55], Hui Zhang[56], Nicholas J. Scott[10], Rachel A. Matson[10], Andrew W. Mann[57], Diana Dragomir[58], Max Günther[21,62], Eric B. Ting[10], Ana Glidden[21], and Elisa V. Quintana[32]

[1] Department of Astronomy, The Ohio State University, 140 West 18th Avenue, Columbus, OH 43210, USA; rodriguezmartinez.2@buckeyemail.osu.edu
[2] Center for Astrophysics, Harvard & Smithsonian, 60 Garden Street, Cambridge, MA 02138, USA
[3] Instituto de Astronomia, Geofísica e Ciencias Atmosféricas, Universidade de São Paulo, Rua do Matão 1226, Cidade Universitária, São Paulo, SP 05508-900, Brazil
[4] Department of Physics, The University of Texas at Dallas, 800 West Campbell Road, Richardson, TX 75080-3021, USA
[5] Perth Exoplanet Survey Telescope, Australia
[6] Department of Physics and Astronomy, Georgia State University, Atlanta, GA 30302, USA
[7] Department of Physics and Astronomy, University of Louisville, Louisville, KY 40292, USA
[8] University of Southern Queensland, Centre for Astrophysics, West Street, Toowoomba, QLD 4350, Australia
[9] The Observatories of the Carnegie Institution for Science, 813 Santa Barbara Street, Pasadena, CA 91101, USA
[10] NASA Ames Research Center, Moffett Field, CA 94035, USA
[11] Caltech IPAC—NASA Exoplanet Science Institute, 1200 East California Avenue, Pasadena, CA 91125, USA
[12] Dunlap Institute for Astronomy and Astrophysics, University of Toronto, ON M5S 3H4, Canada
[13] Department of Physics and Astronomy, Vanderbilt University, Nashville, TN 37235, USA
[14] Department of Physics, Fisk University, 1000 17th Avenue North, Nashville, TN 37208, USA
[15] Las Cumbres Observatory, 6740 Cortona Drive, Suite 102, Goleta, CA 93117, USA
[16] Gemini Observatory, Northern Operations Center, 670 North A'ohoku Place, Hilo, HI 96720, USA
[17] Department of Astronomy and Steward Observatory, University of Arizona, Tucson, AZ 85721, USA
[18] Department of Astrophysical Sciences, Princeton University, 4 Ivy Lane, Princeton, NJ 08544, USA
[19] School of Physics, Sydney Institute for Astronomy (SIfA), The University of Sydney, NSW 2006, Australia
[20] Department of Physics, Lehigh University, 16 Memorial Drive East, Bethlehem, PA 18015, USA
[21] Department of Physics and Kavli Institute for Astrophysics and Space Research, Massachusetts Institute of Technology, Cambridge, MA 02139, USA
[22] Department of Astronomy & Astrophysics, The Pennsylvania State University, 525 Davey Lab, University Park, PA 16802, USA
[23] Center for Exoplanets and Habitable Worlds, The Pennsylvania State University, 525 Davey Lab, University Park, PA 16802, USA
[24] Department of Physics and Astronomy, Swarthmore College, Swarthmore, PA 19081, USA
[25] Department of Terrestrial Magnetism, Carnegie Institution for Science, 5241 Broad Branch Road, NW, Washington, DC 20015, USA
[26] Cerro Tololo Inter-American Observatory, Casilla 603, La Serena, Chile
[27] National Optical Astronomy Observatory, 950 North Cherry Avenue, Tucson, AZ 85719, USA
[28] Exoplanetary Science at UNSW, School of Physics, UNSW Sydney, NSW 2052, Australia
[29] Department of Physics, University of Warwick, Gibbet Hill Road, Coventry CV4 7AL, UK
[30] Centre for Exoplanets and Habitability, University of Warwick, Gibbet Hill Road, Coventry CV4 7AL, UK
[31] American Association of Variable Star Observers, 49 Bay State Road, Cambridge, MA 02138, USA
[32] Exoplanets and Stellar Astrophysics Laboratory, Code 667, NASA Goddard Space Flight Center, Greenbelt, MD 20771, USA
[33] Ivan Curtis Private Observatory, Australia
[34] George P. and Cynthia Woods Mitchell Institute for Fundamental Physics and Astronomy, Texas A&M University, College Station, TX 77843, USA
[35] Department of Physics and Astronomy, Texas A&M University, College Station, TX 77843, USA
[36] El Sauce Observatory, Chile
[37] Atalaia Group & CROW Observatory, Portalegre, Portugal
[38] Department of Physics & Astronomy, University of Wyoming, 1000 East University Avenue, Department 3905, Laramie, WY 82071, USA
[39] Black Hole Initiative at Harvard University, 20 Garden Street, Cambridge, MA 02138, USA
[40] Department of Physics and Astronomy, Brigham Young University, Provo, UT 84602, USA
[41] South African Astronomical Observatory, P.O. Box 9, Observatory, 7935, Cape Town, South Africa
[42] Southern African Large Telescope, P.O. Box 9, Observatory, 7935, Cape Town, South Africa
[43] Spot Observatory, Nashville, TN 37206, USA
[44] Department of Astronomy, Wellesley College, Wellesley, MA 02481, USA

* This paper includes data gathered with the 6.5 m Magellan Telescopes located at Las Campanas Observatory, Chile.

[45] Department of Physics and Astronomy, Louisiana State University, Baton Rouge, LA 70803, USA
[46] Department of Physical Sciences, Kutztown University, Kutztown, PA 19530, USA
[47] Hazelwood Observatory, Churchill, VIC, Australia
[48] Winer Observatory, P.O. Box 797, Sonoita, AZ 85637, USA
[49] Società Astronomica Lunae, Italy
[50] Department of Earth, Atmospheric and Planetary Sciences, Massachusetts Institute of Technology, Cambridge, MA 02139, USA
[51] Department of Aeronautics and Astronautics, MIT, 77 Massachusetts Avenue, Cambridge, MA 02139, USA
[52] Department of Astronomy, The University of Texas at Austin, Austin, TX 78712, USA
[53] Department of Earth Sciences, University of California, Riverside, CA 92521, USA
[54] Department of Astronomy, University of Florida, 211 Bryant Space Science Center, Gainesville, FL 32611, USA
[55] George Mason University, 4400 University Drive MS 3F3, Fairfax, VA 22030, USA
[56] School of Astronomy and Space Science, Key Laboratory of Modern Astronomy and Astrophysics in Ministry of Education, Nanjing University, Nanjing 210046, Jiangsu, People's Republic of China
[57] Department of Physics and Astronomy, University of North Carolina at Chapel Hill, Chapel Hill, NC 27599, USA
[58] Department of Physics and Astronomy, University of New Mexico, 1919 Lomas Boulevard NE, Albuquerque, NM 87131, USA
Received 2019 December 2; revised 2020 June 16; accepted 2020 June 17; published 2020 August 14

Abstract

We present the discoveries of KELT-25 b (TIC 65412605, TOI-626.01) and KELT-26 b (TIC 160708862, TOI-1337.01), two transiting companions orbiting relatively bright, early A stars. The transit signals were initially detected by the KELT survey and subsequently confirmed by Transiting Exoplanet Survey Satellite (TESS) photometry. KELT-25 b is on a 4.40 day orbit around the $V = 9.66$ star CD-24 5016 ($T_{\rm eff} = 8280^{+440}_{-180}$ K, $M_\star = 2.18^{+0.12}_{-0.11}\ M_\odot$), while KELT-26 b is on a 3.34 day orbit around the $V = 9.95$ star HD 134004 ($T_{\rm eff} = 8640^{+500}_{-240}$ K, $M_\star = 1.93^{+0.14}_{-0.16}\ M_\odot$), which is likely an Am star. We have confirmed the substellar nature of both companions through detailed characterization of each system using ground-based and TESS photometry, radial velocity measurements, Doppler tomography, and high-resolution imaging. For KELT-25, we determine a companion radius of $R_{\rm P} = 1.64^{+0.039}_{-0.043}\ R_{\rm J}$ and a 3σ upper limit on the companion's mass of $\sim$64 $M_{\rm J}$. For KELT-26 b, we infer a planetary mass and radius of $M_{\rm P} = 1.41^{+0.43}_{-0.51}\ M_{\rm J}$ and $R_{\rm P} = 1.94^{+0.060}_{-0.058}\ R_{\rm J}$. From Doppler tomographic observations, we find KELT-26 b to reside in a highly misaligned orbit. This conclusion is weakly corroborated by a subtle asymmetry in the transit light curve from the TESS data. KELT-25 b appears to be in a well-aligned, prograde orbit, and the system is likely a member of the cluster Theia 449.

Unified Astronomy Thesaurus concepts: Exoplanet astronomy (486); Transit photometry (1709); Radial velocity (1332)

Supporting material: data behind figures

1. Introduction

The field of exoplanets has grown tremendously since the first detection of a transiting exoplanet around a bright star (Charbonneau et al. 2000; Henry et al. 2000) two decades ago. Thousands of planets[63] have been validated orbiting stars of almost every spectral type and span a wide range of masses, orbits, and likely compositions. Our knowledge of the demographics of short-period giant exoplanets quickly expanded with the advent of dedicated wide-field transit surveys from the ground, such as the Hungarian-made Automated Telescope Network (HATNet; Bakos et al. 2007), the HATSouth survey (Bakos et al. 2013), the Wide Angle Search for Planets (WASP/SuperWASP; Pollacco et al. 2006; Collier Cameron et al. 2009), the Qatar Exoplanet Survey (QES; Alsubai et al. 2011), XO (McCullough et al. 2005), the Trans-Atlantic Exoplanet Survey network (TrES; Alonso et al. 2007), and the Kilodegree Extremely Little Telescope (KELT; Pepper et al. 2007, 2012), to mention a few.

The Kepler space telescope (Borucki et al. 2010) provided the first statistical survey of a large number of transiting planets over a broad region of radius and orbital period. Kepler transformed our understanding of the population of relatively short-period ($P \lesssim 100$ days) planets. Later, the next generation of dedicated wide-field surveys came online, such as the Next Generation Transit Survey (NGTS; Bayliss et al. 2018) and the Multi-site All-Sky CAmeRA (MASCARA; Lesage et al. 2014). In addition, based largely on arguments presented in Gould et al. (2003) and Blake et al. (2007), targeted ground-based surveys were initiated, such as MEarth (Nutzman & Charbonneau 2008; Charbonneau et al. 2009; Berta et al. 2012), TRAPPIST (Gillon et al. 2017), and SPECULOOS (Delrez et al. 2018), which primarily concentrate their efforts on the search for exoplanets around low-mass stars.

Hot stars with large radii are typically avoided by targeted transit surveys because planets around them induce weaker photometric signals. More importantly, the host stars have fewer spectral lines, and the lines they do have are significantly broadened by their fast rotation. A large fraction of stars above the Kraft break ($T_{\rm eff} \gtrsim 6250$ K; Kraft 1967) are observed to rotate significantly faster ($v \sin I_* \geqslant 10$ km s^{-1}) than cooler stars. This is because stars with $T_{\rm eff} \gtrsim 6250$ K have essentially no convective envelopes and thus do not slow down due to magnetic braking over their evolution. They therefore essentially retain their high primordial spin rates. The relative

[59] NASA Hubble Fellow.
[60] Pappalardo Fellow.
[61] Eberly Fellow.
[62] Juan Carlos Torres Fellow.
[63] Over 4100, as of 2020 (https://exoplanetarchive.ipac.caltech.edu/).

paucity of spectral features coupled with their faster rotation rates make candidate planetary companions transiting hot stars harder to confirm using the radial velocity (RV) method (see, e.g., Johnson et al. 2018 and Dholakia et al. 2019). To attempt to circumvent the challenges in searching for planets around massive stars on the main sequence, a number of RV surveys have studied "retired A stars"—cooler, evolved stars that have moved off the main sequence. Such surveys have yielded a number of discoveries (e.g., Johnson et al. 2007, 2011; Hatzes et al. 2018) but have only been able to sample a relatively small number of target stars due to the focused nature of RV studies.

Despite the observational challenges posed by hot stars, they provide opportunities to study the most massive, highly irradiated, close-in planets, in particular the relatively new category of "ultrahot Jupiters" (Collier Cameron et al. 2010). Ultrahot Jupiters provide a unique opportunity for the detailed atmospheric characterization of highly irradiated giant planets. They have high equilibrium temperatures, allowing one to probe extreme conditions that are not present in the solar system. In particular, many of these ultrahot Jupiters have dayside temperatures that are hot enough to disassociate all molecules, leaving atomic metals as the dominant species on the dayside (Gaudi et al. 2017). Furthermore, the exceptionally high dayside temperatures of these planets imply that they are typically close to chemical equilibrium (Kitzmann et al. 2018), making the interpretation of observations much simpler and resulting in atmospheres that are likely quite different than typical hot Jupiters (Bell & Cowan 2018; Kitzmann et al. 2018; Lothringer et al. 2018). In addition, A-type hosts present opportunities to test the effects of host star mass and binarity and short evolutionary timescales on giant planet formation, evolution, and engulfment by their host stars. For example, a recent study found that most giant planets around A-type stars are eventually engulfed by their host stars (Stephan et al. 2018), and a related study determined the observable effects of engulfment (Stephan et al. 2020). In general, the high temperatures and scale heights of ultrahot Jupiters make follow-up observations much easier, allowing one to test models of hot Jupiter atmospheres (e.g., Cauley et al. 2019; Hoeijmakers et al. 2019).

Studying the planetary population of massive (A) stars is also interesting for other reasons. First, the large amount of high-energy radiation they emit helps to test theories of planet atmospheric evaporation. Second, the fact that A stars tend to be rapidly rotating means that they are typically oblate, resulting in significant gravity darkening, which can be used to estimate the true (not just projected) spin–orbit angle of the planet (Barnes 2009). The oblateness of the host star, combined with certain orbital alignments of the planet, can result in relatively short precession times of the planetary orbit (Johnson et al. 2015). Finally, their short lifetimes imply that the lifetimes of close-in planets orbiting such stars are likely to be much shorter than those of such planets orbiting low-mass stars (Stephan et al. 2018).

Royer et al. (2007) found that typical rotational values ($v \sin I_*$) are greater than 100 km s^{-1} for stars in the the B9–F2 spectral range (for reference, the Sun's rotational velocity is only 1.6 ± 0.3 km s^{-1}; Pavlenko et al. 2012). Because of the difficulties in confirming planets orbiting these fast rotators, KELT routinely uses a combination of RV and Doppler tomographic observations (Collier Cameron et al. 2010). Doppler tomography (DT) measures the distortion in the spectral lines of a star caused by the transiting planet blocking the light from the star with different projected velocities as it crosses the disk of the star. Doppler tomographic observations can help confirm that the planet transits the target star and is not, for example, a signal from a nearby eclipsing binary, although confirming the planetary nature of the occultor also requires an appropriately stringent upper limit on its mass (see, e.g., Bieryla et al. 2015 for a discussion of validating planets orbiting rapidly rotating stars using DT). The advantage of this technique is that it is better suited to faster stellar rotations, thereby providing an alternative way to confirm planets around hot stars. Many discovery papers have demonstrated that A-type stars are the most suitable for the measurement of the Rossiter–McLaughlin (RM) effect because they have the optimal combination of R_p/R_s and rotation—two parameters to which the RM signal is proportional (see also Gaudi & Winn 2007; Triaud 2018, and Table 8 of this paper).

With DT, we can not only validate new planets but also determine their projected spin–orbit angles, λ. From the current sample of over 200 systems[64] with measured λ, a dichotomy in stellar temperature has emerged: giant planets around cool stars ($T_{\rm eff} < 6200$ K) have lower obliquities than those around hot stars (Schlaufman 2010; Winn 2010; Dawson et al. 2015). In addition, the most massive planets ($M_p > 3\ M_J$) tend to have lower spin–orbit angles (Hébrard et al. 2010). These results are important because they help constrain planet formation and migration mechanisms for hot Jupiters. One area of ongoing research is the question of whether hot Jupiters form "in situ" or at larger separations from their host and then migrate into their present observed locations via planet–disk or planet–planet dynamical or secular interactions with a distant planetary, brown dwarf, or stellar companion (e.g., Dawson & Johnson 2018). Measurements of λ provide insights into these formation channels, since different theories predict different values of the distribution of spin–orbit angles. In addition, star–planet interactions can also shape the distribution of λ.

Giant planets at close separations are highly irradiated by their host stars, and this intense radiation can significantly impact their properties. One possible consequence is radius inflation: it has been observed that hot Jupiters' radii appear to increase with increasing incident radiation from the host star (Demory & Seager 2011; Howell et al. 2019), although it is not clear whether this is caused by the radiation reinflating the planet or because it simply slows the cooling and contraction process of the planets, which may be hot and thus inflated upon formation.

In this paper, we present the discoveries of a substellar companion and likely planet (KELT-25 b) and a hot Jupiter (KELT-26 b[65]), both orbiting bright, early A stars, first identified as candidates in KELT data and subsequently observed by the Transiting Exoplanet Survey Satellite (TESS) mission. Although the TESS mission's main science driver is to measure small planets, simulations have estimated yields of

[64] https://www.astro.keele.ac.uk/jkt/tepcat/obliquity.html

[65] While we were writing this manuscript, we noted a paper on arXiv in which WASP announced the discovery of WASP-178b (Hellier et al. 2019). We had already collected and analyzed the data needed to confirm KELT-26 b, and other than to confirm that KELT-26 and WASP-178 had the same coordinates, we did not read or use the results of Hellier et al. (2019) in any way. We therefore claim an independent discovery (regardless of whether or not they are the same planet). If they are the same planet, we do not, of course, claim to be the first to have made the detection.

thousands of giant planets, which include Jupiter-sized planets around bright stars (e.g., Barclay et al. 2018). TESS's expected yield complements the discoveries made by KELT and other ground-based surveys and advances our understanding of giant planets around hot stars.

2. Discovery and Follow-up Observations

2.1. KELT Discovery

One survey that has contributed significantly to the discovery and study of ultrahot Jupiters is KELT[66] (Pepper et al. 2007). KELT observes ∼85% of the sky, targeting bright stars in the magnitude range $7.5 < V < 12$ and filling in the gap between RV surveys and other transit surveys, which generally focus on brighter and fainter stars, respectively. KELT consists of two observatories: KELT-South (KS; Pepper et al. 2012), located in Sutherland, South Africa, which surveys most of the southern hemisphere, and KELT-North (KN; Pepper et al. 2007, 2013), which observes the northern hemisphere from Sonoita, Arizona. Each observing site has a Mamiya 645 80 mm f/1.9 42 mm lens with a $4k \times 4k$ Apogee CCD on a Paramount ME mount. The KELT telescopes have a 23″ pixel scale, a 26° × 26° field of view, and a 20–30 minute cadence. The original goal of the KELT survey was to discover hot Jupiters orbiting bright host stars, which are amenable to detailed characterization through transmission or eclipse spectroscopy. More recently, KELT has become a significant contributor to the understanding of planets around early-type stars, discovering 24 planets, of which six are hot Jupiters around A stars, including the planets presented here (Zhou et al. 2016; Gaudi et al. 2017; Lund et al. 2017; Johnson et al. 2018; Siverd et al. 2018).

The likely planetary companion orbiting TIC 65412605 (hereafter KELT-25 b) was first identified as a planet candidate following the reduction of KS field KS35. KELT-25 is located at $\alpha_{J2000} = 07^h12^m29\overset{s}{.}55$, $\delta_{J2000} = -24°57'12''82$ (Gaia Collaboration et al. 2018), and KS survey field 35 is centered at $\alpha_{J2000} = 07^h40^m12\overset{s}{.}0$, $\delta_{J2000} = -20°00'00\overset{''}{.}0$. The field KS35 was observed 2860 times from UT 2013 May 10 to 2017 October 1.

The image reduction and candidate selection pipeline are described in detail in Siverd et al. (2012) and Kuhn et al. (2016) and briefly summarized here. To reduce the raw survey images, KELT uses a modified image subtraction pipeline based on the ISIS software (Alard & Lupton 1998; Alard 2000). The list of sources identified in the KELT fields are then cross-matched to the Tycho-2 (Høg et al. 2000) and UCAC4 (Zacharias et al. 2013) catalogs to obtain their proper motions. We then implement reduced proper motion (RPM) cuts to identify and exclude giants before searching for transit signals (Gould & Morgan 2003; Collier Cameron et al. 2007). Finally, we search for transit-like features in all stars that passed the RPM cuts using the box-fitting least-squares (BLS) algorithm (Kovács et al. 2002).

The planet orbiting TIC 160708862 (hereafter KELT-26 b) is located at $\alpha_{J2000} = 15^h09^m04\overset{s}{.}89304$, $\delta_{J2000} = -42°42'17''78910$ (Gaia Collaboration et al. 2018) in the KS37 field, which is centered at $\alpha_{J2000} = 15^h07^m12\overset{s}{.}00$, $\delta_{J2000} - 53°00'00''00$. This field was observed 2085 times from UT 2013 September 5 to 2015 September 11.

[66] https://keltsurvey.org

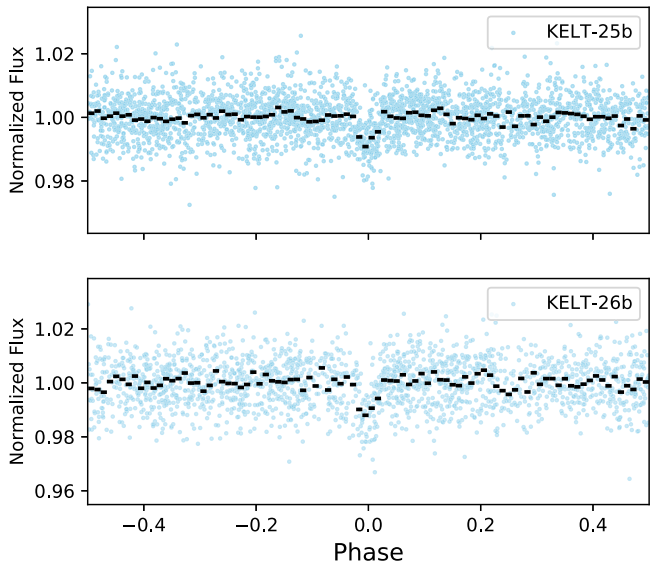

Figure 1. Discovery light curves for KELT-25 b (top) and KELT-26 b (bottom) from the KS telescope. The light curves are phase-folded on the preliminary orbital periods of 4.401093 (KELT-25 b) and 3.344886 (KELT-26 b) days. The blue points represent the data, and the black points are the data binned at intervals of 0.01 in phase.

Both companions were identified as candidates from a periodicity search using the BLS algorithm. KELT-25 b was initially identified with a BLS orbital period of 4.40 days and a transit depth of 0.66%, while KELT-26 b was detected with a period of 3.34 days and a 1.1% transit depth. The phase-folded KELT discovery light curves are shown in Figure 1. See Table 1 for literature information about the stellar hosts KELT-25 and KELT-26.

2.2. TESS Photometry

The NASA TESS mission (Ricker et al. 2015) was launched on 2018 April 18 with the primary goal of discovering and characterizing small ($R_p < 4R_\oplus$) exoplanets around bright nearby stars. Presently, dozens of exoplanets have already been validated, while almost 1000 candidates await confirmation. The confirmed systems include a few giant planets on short-period orbits (Brahm et al. 2019; Nielsen et al. 2019; Rodriguez et al. 2019b).

KELT-25 was observed in sector 7 by camera 2 of the TESS spacecraft between UT 2019 January 7 and February 7. TESS will observe KELT-25 again in sectors 33 and 34 (2020 December 17–2021 February 9).

We made use of the 30 minute cadence full-frame images (FFIs) made available by the Mikulski Archive for Space Telescopes (MAST) and calibrated by the Science Processing Operations Center (SPOC) pipeline (Jenkins et al. 2016). Cutouts of 10 × 10 pixels were extracted from the FFIs around each target star via the MAST *TESScut* tool, and aperture photometry was performed using the *lightkurve* package (Lightkurve Collaboration et al. 2018; Barentsen et al. 2019). To evaluate the background flux, we used an aperture around the target star encompassing pixels with fluxes higher than 90% of the rest of the pixels in the cutout, as well as pixels that did not encompass adjacent stars. We accounted for dilution within the TESS aperture by computing for and removing the light contribution of known nearby stars, as per their TESS band magnitudes in the TIC.

Table 1
Literature Properties for KELT-25 and KELT-26

Parameter	Description	KELT-25	KELT-26	Source
Other identifiers		CD-24 5016 TIC 65412605 TYC 6528-1639-1	HD 134004 TIC 160708862 TYC 7829-2324-1	
α_{J2000}	R.A.	07:12:29.55004	15:09:04.89304	1
δ_{J2000}	decl.	−24:57:12.82193	−42:42:17.78910	1
l	Galactic longitude	237.°5346109	328.°1938368	1
b	Galactic latitude	−6.°79674034	+13.°3150904	1
B_T	Tycho B_T mag.	9.841 ± 0.019	10.083 ± 0.028	2
V_T	Tycho V_T mag.	9.655 ± 0.018	9.961 ± 0.033	2
G	Gaia G mag.	9.5960 ± 0.0003	9.912 ± 0.020	1
J	2MASS J mag.	9.362 ± 0.03	9.775 ± 0.030	3
H	2MASS H mag.	9.273 ± 0.02	9.735 ± 0.020	3
K_S	2MASS K_S mag.	9.248 ± 0.02	9.703 ± 0.020	3
WISE1	WISE1 mag.	9.213 ± 0.022	9.670 ± 0.030	4
WISE2	WISE2 mag.	9.245 ± 0.02	9.683 ± 0.030	4
WISE3	WISE3 mag.	9.302 ± 0.033	9.645 ± 0.043	4
μ_α	Gaia DR2 proper motion in R.A. (mas yr^{-1})	−2.276 ± 0.06	−10.011 ± 0.122	1
μ_δ	Gaia DR2 proper motion in decl. (mas yr^{-1})	0.338 ± 0.075	−5.652 ± 0.097	1
π[a]	Gaia parallax (mas)	2.342 ± 0.043[a]	2.394 ± 0.060[a]	1
RV	Absolute radial velocity (km s^{-1})	35.472±1.011	−24.140 ± 0.045	This work
d	Distance (pc)	427.0 ± 7.8	417.7 ± 10.5	1
U[b]	Space velocity (km s^{-1})	−13.40 ± 0.58	-24.63 ± 0.37	Section 5.1
V	Space velocity (km s^{-1})	−13.83 ± 0.84	6.75 ± 0.58	Section 5.1
W	Space velocity (km s^{-1})	−1.24 ± 0.19	0.78 ± 0.20	Section 5.1

Notes.
[a] Parallaxes here are corrected for the 82 μas offset reported in Stassun & Torres (2018).
[b] Here U is in the direction of the Galactic center.
References. (1) Gaia Collaboration et al. (2018), (2) Høg et al. (2000), (3) Cutri et al. (2003), (4) Zacharias et al. (2017).

Similarly, KELT-26 was observed by TESS between UT 2019 April 22 and May 20 during sector 11 of the mission, and it will be observed again by TESS in sector 38 (2021 April 28 to May 26, in cycle 3). The light-curve extraction for KELT-26 was the same as that described above. Figures 2 and 3 show the raw and reduced TESS light curves for KELT-25 b and KELT-26 b.

2.3. Ground-based Photometry from the KELT Follow-up Network

In order to confirm that the transit signals are due to bona fide planetary companions, rule out false positives such as eclipsing binaries, and refine the transit depth, duration, and ephemeris of our candidates, we obtained photometric observations of KELT-25 b and KELT-26 b from the KELT Follow-Up Network (KELT-FUN; Collins et al. 2018). Some of the follow-up photometry was reduced using the `AstroImageJ` analysis software (Collins et al. 2017). See Table 2 for technical information about the observatories that followed up these systems. The KELT-FUN transits for both systems are shown in Figures 4 and 5.

2.3.1. Perth Exoplanet Survey Telescope

The Perth Exoplanet Survey Telescope (PEST) home observatory was built in 2010 and has since helped discover dozens of exoplanets, including KELT candidates, mostly via the transit method. It is located in Perth, Australia, and is owned and run by Thiam-Guan Tan. The instrument is a 0.3 m Meade LX200 SCT f/10 and focal reducer yielding f/5. The camera is an SBIG ST-8XME with multiple filters including I, and it has a field of view of $31' \times 21'$ and an image scale of $1.''2$ pixel^{-1}. PEST observed a full transit of KELT-25 b in the R_c filter on UT 2019 January 18 and a full transit of KELT-26 b in the I filter on UT 2016 August 26.

2.3.2. Mt. Kent CDK700 Telescope

Photometric follow-up of KELT-26 was taken with the University of Louisville's Shared Skies MKO-CDK700 telescope at Mt. Kent Observatory of the University of Southern Queensland, Australia. The instrument is a 0.7 m Planewave-corrected Dall-Kirkham (CDK) telescope with a Nasmyth focus. The telescope was used with an Apogee U16 CCD camera (Kodak KAF-16801E sensor). The CDK700 telescope

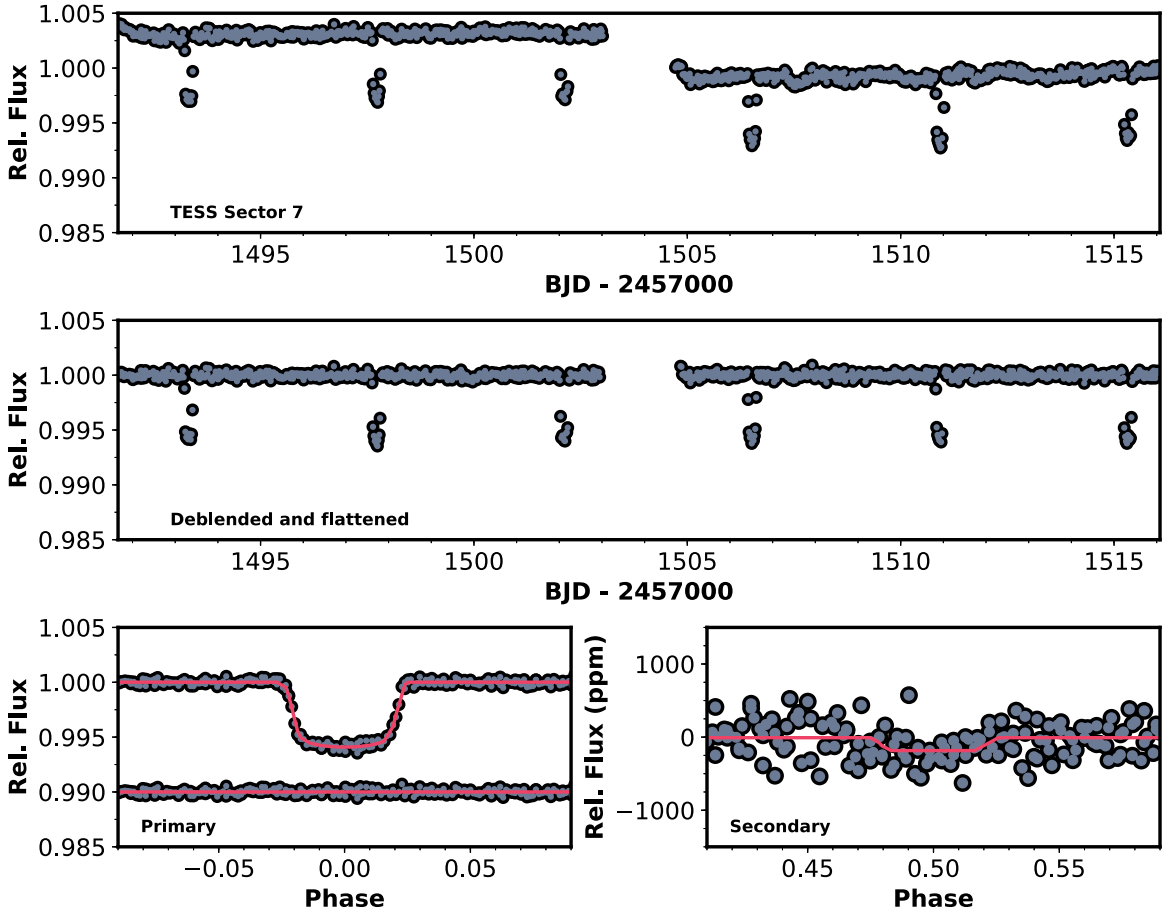

Figure 2. TESS light curve of KELT-25. The top panel shows the raw light curve; the middle panel shows the detrended light curve. The bottom left panel shows the transit and best-fit EXOFASTv2 model to the detrended light curve, phase-folded on the orbital period, with residuals plotted below the transit. The bottom right panel shows the region of the secondary eclipse, which is clearly detected in TESS.

observed a full transit of KELT-26 b, acquiring 165 images in the Sloan r' filter on UT 2018 March 20.

3. Spectroscopic Observations

3.1. TRES Spectroscopy of KELT-25

To constrain the planet mass and characterize the host star properties of KELT-25, we made a series of spectroscopic observations with the Tillinghast Reflector Echelle Spectrograph (TRES; Fűrész 2008) on the 1.5 m telescope at the Fred Lawrence Whipple Observatory (FLWO) in Arizona, USA. TRES is a fiber-fed echelle spectrograph with a resolving power of $\lambda/\Delta\lambda \equiv R = 44{,}000$ spanning 3850–9100 Å. A series of spectra were obtained for KELT-25 over 10 epochs with exposure times of 800 s for a signal-to-noise ratio (S/N) of ∼51 from UT 2019 January 26 to 2019 May 20. These observations are reduced via the procedure described in Buchhave et al. (2012), and relative velocities were obtained via a multi-order cross-correlation against an averaged observed spectral template, as per Quinn et al. (2012). The relative RVs are listed in Table 3 and plotted in Figure 6.

To establish the absolute systemic velocity of the system, we cross-correlated the Mg *b* line order of one of the observed spectra against a synthetic template and shifted all other velocities relative to this template.

While we measure the reflex Doppler signal from KELT-26 to $\sim\sigma_K/K \simeq 30\%$ and thus are able to constrain the mass of KELT-26 b, we do not obtain a definitive detection of the reflex Doppler signal from KELT-25 and thus are only able to provide an upper limit on the planet mass.

3.2. CHIRON Spectroscopy of KELT-25 and KELT-26

We obtained a series of spectroscopic observations of KELT-25 and KELT-26 with the CHIRON spectrograph on the SMARTS 1.5 m telescope, located at the Cerro Tololo Inter-American Observatory (CTIO), Chile. CHIRON is a fiber-fed echelle spectrograph, sliced via an image slicer, yielding a resolving power of $R = 80{,}000$ over the wavelength range 4100–8700 Å (Tokovinin et al. 2013). Wavelength calibrations are provided by bracketing thorium–argon (Th–Ar) arc lamp exposures.

We used CHIRON to measure the spectroscopic orbit and characterize the host star of KELT-26 b. A total of 15 CHIRON epochs covering all orbital phases of KELT-26 b were obtained with an exposure time of ∼1800 s for an S/N of 135. Relative velocities were measured from each spectrum by deriving their stellar line broadening kernels via a least-squares deconvolution (LSD) analysis (described in Zhou et al. 2016). These velocities are listed in Table 4, and Figure 6 shows the RVs as a function of time and phase-folded by the photometric ephemeris.

The absolute RV was estimated by comparing the systemic velocity of KELT-26 in the native CHIRON system to that of four RV standard stars observed by CHIRON in order to

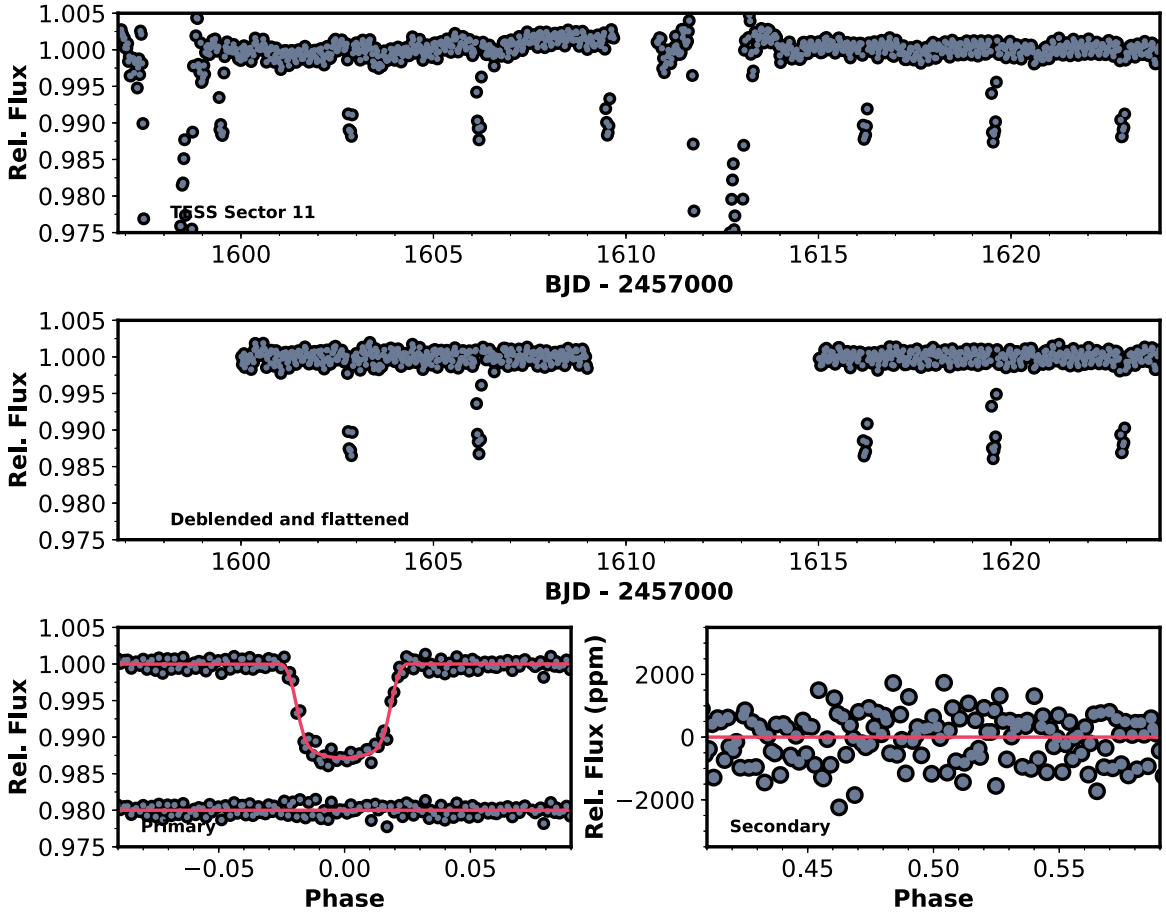

Figure 3. TESS light curve of KELT-26. The top panel shows the raw light curve; the middle panel shows the detrended light curve, where some data were discarded due to momentum dumps and scattered light. The bottom left panel shows the transit and best-fit EXOFASTv2 model to the detrended light curve, phase-folded on the orbital period, with residuals plotted below the transit. The bottom right plot shows the region of the secondary eclipse. While the secondary eclipse is not detected in the TESS data, the primary phase-folded transit shows evidence for a slight asymmetry, which is likely real and may be caused by gravity darkening of the star. However, the primary also shows periodic photometric oscillations at a period that is nearly commensurate (1:18) with the period of the planet. This variability may also be causing the slight asymmetry.

determine a mean offset of -1.455 ± 0.037 km s^{-1} of KELT-26 systemic velocity relative to the CHIRON system. We added the uncertainty in the systemic velocity in the CHIRON system of 0.025 km s^{-1} in quadrature to arrive at a final absolute systemic velocity of -1.455 ± 0.045 km s^{-1}. We corrected the individual CHIRON relative velocities and uncertainties in the same way.

We also used CHIRON to observe the spectroscopic transit of KELT-25 b on UT 2019 May 21. A total of 18 spectra were obtained covering the transit, with an integration time of 600 s exposure^{-1} for an S/N of 75. Spectral line profiles were derived from each spectrum as per the procedure described in Section 3.3. The spectroscopic shadow (i.e., DT signal) of the transiting companion is shown in Figure 7.

3.3. Spectroscopic Transit of KELT-25 with the PFS

We monitored a transit of KELT-25 b with the Planet Finding Spectrograph (PFS; Crane et al. 2010) on the 6.5 m Magellan-Clay telescope at Las Campanas Observatory, Chile. A total of 19 spectra were obtained on UTC 2019 April 21 spanning 3.3 hr, each observation with an integration time of 600 s for an S/N ranging from 52 to 58. For our observations, PFS was fed by a 0.″3 slit, yielding a spectral resolving power of $R = 130{,}000$ over the wavelength region 3910–7340 Å. To enable better derivation of the stellar line profiles, the iodine cell was omitted from our observations. Wavelength calibrations were provided by Th–Ar hollow cathode lamp observations obtained at the beginning and end of the night.

Stellar line profiles were derived from each spectrum as per Donati et al. (1997) and Collier Cameron et al. (2010) via an LSD analysis of the spectra against a nonrotating synthetic template spectrum generated via the ATLAS9 model atmospheres (Castelli & Kurucz 2003). During the transit, the planet sequentially blocks parts of the rotating stellar disk, casting a shadow in our observed rotationally broadened line profiles of the star. When we subtract an averaged line profile from each observation, the residuals reveal the spectroscopic transit of the planet as a shadow traversing across the stellar surface. The line profile residuals and best-fitting models are shown in Figure 7.

3.4. Spectroscopic Transit of KELT-26 with MINERVA-Australis

To measure the orbital obliquity and confirm the planetary status of KELT-26 b, we obtained a series of spectroscopic observations during its transit on UT 2019 June 18 with the MINiature Exoplanet Radial Velocity Array (MINERVA-Australis) facility, located at the University of Southern Queensland's Mt. Kent Observatory, Australia (Addison et al. 2019). At the time of

Table 2
Follow-up Photometric Observations of KELT-25 b and KELT-26 b

Target	Observatory	Date (UT)	Diameter (m)	Filter	FOV	Pixel Scale	Exposure (s)
KELT-25 b	PEST	2019 Jan 18	0.3	*Rc*	$31' \times 21'$	$1\farcs2$	30
KELT-25 b	TESS	2019 Jan 7–2019 Feb 7	0.105	TESS (600–1000 nm)	$24° \times 24°$	$21''$	1800
KELT-26 b	PEST	2016 Aug 26	0.3	*I*	$31' \times 21'$	$1\farcs2$	30
KELT-26 b	Mt. Kent CDK700	2018 Mar 20	0.6858	r'	$27\farcm3 \times 27\farcm3$	$0\farcs4$	65
KELT-26 b	TESS	2019 Apr 22–2019 May 20	0.105	TESS (600–1000 nm)	$24° \times 24°$	$21''$	1800

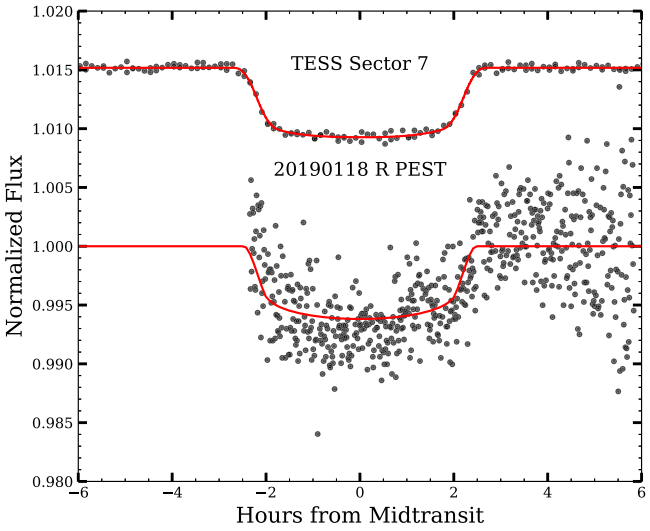

Figure 4. Follow-up and TESS light curves of KELT-25. The bottom transit shows the KELT-FUN light curve phase-folded to the ephemeris determined in the global fit (Table 6). Table 2 contains information on all of the follow-up observations. The black points are the relative fluxes, while the red line shows the EXOFASTv2 model.

(The data used to create this figure are available.)

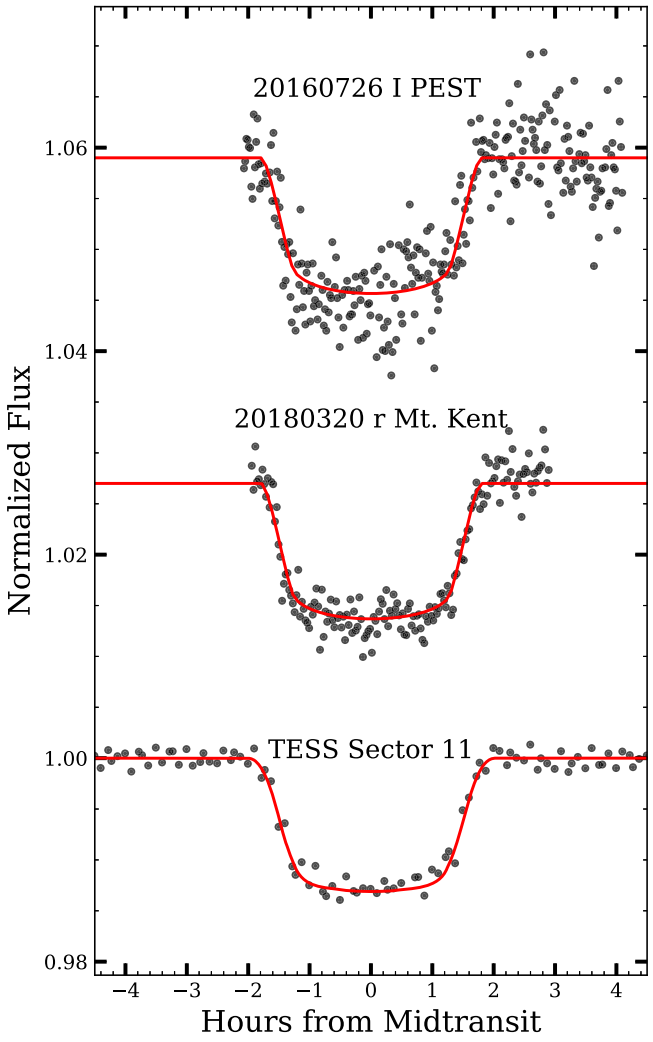

Figure 5. Follow-up and TESS light curves of KELT-26. The top two transits show the KELT-FUN light curves phase-folded to the ephemeris determined in the global fit (Table 6). Table 2 contains information on all of the follow-up observations. The black points are the relative fluxes, while the red line shows the EXOFASTv2 model.

(The data used to create this figure are available.)

observations, MINERVA-Australis was operating three active 0.7 m telescopes feeding into a single Kiwispec echelle spectrograph, yielding a resolving power of $R = 80{,}000$ over the wavelength region 5000–6300 Å. We made use of data from the two of the three telescopes that yielded the highest S/N spectra on the night of the transit (S/N $\sim$ 16). Spectral line profiles were derived from each spectrum via the LSD analysis described in Section 3.3. From these observations, we detect the spectroscopic shadow of the transit, finding that the path of the planet is offset from but perpendicular to the projected stellar equator. The spectroscopic transit of KELT-26 b is shown in Figure 7.

4. High-resolution Imaging of KELT-25 b and KELT-26 b

4.1. Gemini-South Zorro Speckle

We obtained high-resolution speckle images of KELT-25 and KELT-26 to search for nearby companions that could contaminate or dilute the light curves and thus affect the interpretation of the planetary radii and to rule out sources of false positives, like background eclipsing binaries.

Both stars were observed using Zorro, a speckle interferometer residing at the Gemini-South Observatory. Zorro observes in two bandpasses simultaneously and is optimized for speckle observations. The observations occurred during instrument commissioning and were the first speckle interferometric science observations made by Zorro. Zorro is a dual-channel imager using two electron-multiplying CCDs (EMCCDs) as the detectors and containing filter wheels providing bandpass-limited observations[67] (see

[67] https://www.gemini.edu/sciops/instruments/alopeke/

Table 3
Relative Out-of-transit RVs for KELT-25 from TRES

BJD_{TDB}	RV ($m\ s^{-1}$)	σ_{RV} ($m\ s^{-1}$)
2,458,509.81953	3601.8	380
2,458,511.84309	1657.2	380
2,458,573.61546	480.7	460
2,458,575.63514	991.1	590
2,458,588.63382	1544.3	420
2,458,589.63349	54.5	450
2,458,591.62656	588.2	420
2,458,592.62509	41.9	590
2,458,593.63010	−2782.7	620

Note. We note that while the RVs have been put on an absolute scale for the CHIRON data, there is an additional systematic uncertainty that would affect all of the data points by the same amount of roughly 40 $m\ s^{-1}$, due to the uncertainties of the standard RV stars used to put the RVs on an absolute scale.

Scott & Howell 2018). The Zorro data were reduced in the standard way as described in Howell et al. (2011) and resulted in spatial reconstructions in each bandpass for KELT-25 and KELT-26 providing high-contrast, high-resolution imaging results.

KELT-25 was observed on UT 2019 May 18 in the blue (562/54 nm) and red (832/40 nm) bandpasses simultaneously. The KELT-25 and KELT-26 observations consisted of three sets of 1000 frames with exposure times of 0.06 s each, coadded together during the data reduction process. Figure 8 shows the speckle reconstructed image for KELT-25. The 562 nm observations (Figure 8, top) show no companion star from 0.″1 out to 1″ within 4–4.5 mag of the source, and the 832 nm observations (Figure 8, bottom) confirm this as well in the red, starting from 0.″1 out to a delta magnitude of 5.

KELT-26 was observed on UT 2019 May 21 in the blue and red bandpasses simultaneously. Figure 9 shows the constraints on possible stellar companions to KELT-26. No stellar companions are detected with angular separation from the primary from 17 mas (562 nm) and 28 mas (832 nm) out to 1.″7 and for contrast limits of ∼4.2 mag (562 nm) and 5–7 mag (832 nm). The black solid line on the contrast curve marks the 5σ detection limit.

4.2. SOAR Speckle

KELT-26 was observed with the speckle camera at the Southern Astrophysical Research (SOAR) 4.1 m telescope on UT 2019 August 12. The instrument and data processing are covered in Tokovinin (2018); a full description of the SOAR-TESS survey can be found in Ziegler et al. (2020). Figure 10 shows the 5σ limit of companion detection, and the inset shows the speckle autocorrelation function (ACF). The speckle ACF is symmetric, but the true quadrant was determined from the shift-and-add image.

A nearby faint companion was detected at an angular separation of 2.″4096 at position angle (PA) 311.°2 and a magnitude difference of 7.1 mag in I_c (central wavelength 824 nm, bandwidth 170 nm). This nearby source was not seen in the Gemini-South Zorro observation.

From the contrast magnitude of the neighbor in I_c, we can estimate its contribution to the flux in the diluted transit light curves. In this case, the contribution of the neighbor is proportional to the ratio of the flux of the secondary to the primary, or 0.14% in I_c. This dilution factor reflects the amount by which the true transit depth is diluted and therefore constrains the true radius of the planet.

Given the blending from the companion, the true depth is larger, and therefore the true radius of the planet is larger (Ciardi et al. 2015). The inferred radius of KELT-26 b from the diluted TESS and KELT-FUN light curves (all of which were blended by the neighbor in their apertures) is probably larger by at most ∼0.55% × 0.14% or, equivalently, 0.002 R_J. This is 0.04σ different from our reported value of the planetary radius; thus, it can be considered negligible and does not change our qualitative results. This is simply because the uncertainty on the radius of the planet is dominated by the uncertainty on the radius of the star, not the depth of the transit.

Finally, we note that it is possible that this faint companion is an artifact, based on the fact that there are no sources at that position and magnitude found in either Gaia DR2 or the TESS Input Catalog version 8 (TIC-8; Stassun et al. 2019). Moreover, if it is a real source, at an angular separation of ∼2.″5, it is unlikely to be a bound companion (see, e.g., Matson et al. 2019).

5. Host Star Properties

5.1. Location and Three-dimensional Motion in the Galaxy and Galactic Population

We determine the location in the Galaxy, the three-dimensional (*UVW*) space motion relative to the local standard of rest, and the inferred population of KELT-25 and KELT-26 using their proper motions, parallaxes, and absolute systemic velocities. Because we have poor metallicity constraints (albeit for different reasons; see the discussion below), we are unable to use this stellar property to help constrain the stellar populations of the hosts. However, given that they are both early A stars, we would be surprised if they have significantly subsolar metallicities.

Using the proper motion, Gaia DR2 parallax (corrected for the Stassun & Torres 2018 systematic offset of −82 μas), and the absolute systemic RV determined as described in Section 3.1, we compute $(U, V, W) = (-13.40 \pm 0.58, -13.83 \pm 0.84, -1.24 \pm 0.19)$ km s^{-1}, correcting for the velocity of the Sun with respect to the local standard of rest as determined by Coşkunoğlu et al. (2011). These velocities imply that the probability of KELT-25 being in the thin disk relative to thick disk is 99.4% using the classification scheme of Bensby et al. (2003). The distance to KELT-25 is 427.0 ± 7.8 pc, and it has Galactic coordinates of $(\ell, b) = (237.^\circ5, -6.^\circ8)$. This implies that its vertical (Z) distance from the Sun is $Z - Z_\odot = -50.6$ pc. Given that the Sun is located at $Z_\odot \simeq 30$ pc above the plane, as determined by the local evolved stellar population according to Bovy (2017), this means that KELT-25 is located only about $Z \simeq 20$ pc below the plane. This is consistent with the scale height of early A stars as determined by Bovy (2017).

Using the same methodology, we computed $(U, V, W) = (-24.63 \pm 0.37, 6.75 \pm 0.58, 0.78 \pm 0.20)$ km s^{-1} for KELT-26. These velocities imply that the probability of KELT-26 being in the thin disk relative to the thick disk is 99.3% using the classification scheme of Bensby et al. (2003). The distance to KELT-26 is 417.78 ± 10.5 pc, and it has Galactic coordinates of $(\ell, b) = (328.^\circ19, +13.^\circ32)$. This implies that its vertical (Z) distance from the Sun is $Z - Z_\odot = 96.1$ pc and $Z \simeq$ 126 pc above the plane. This is roughly twice the typical scale height of an early A star as

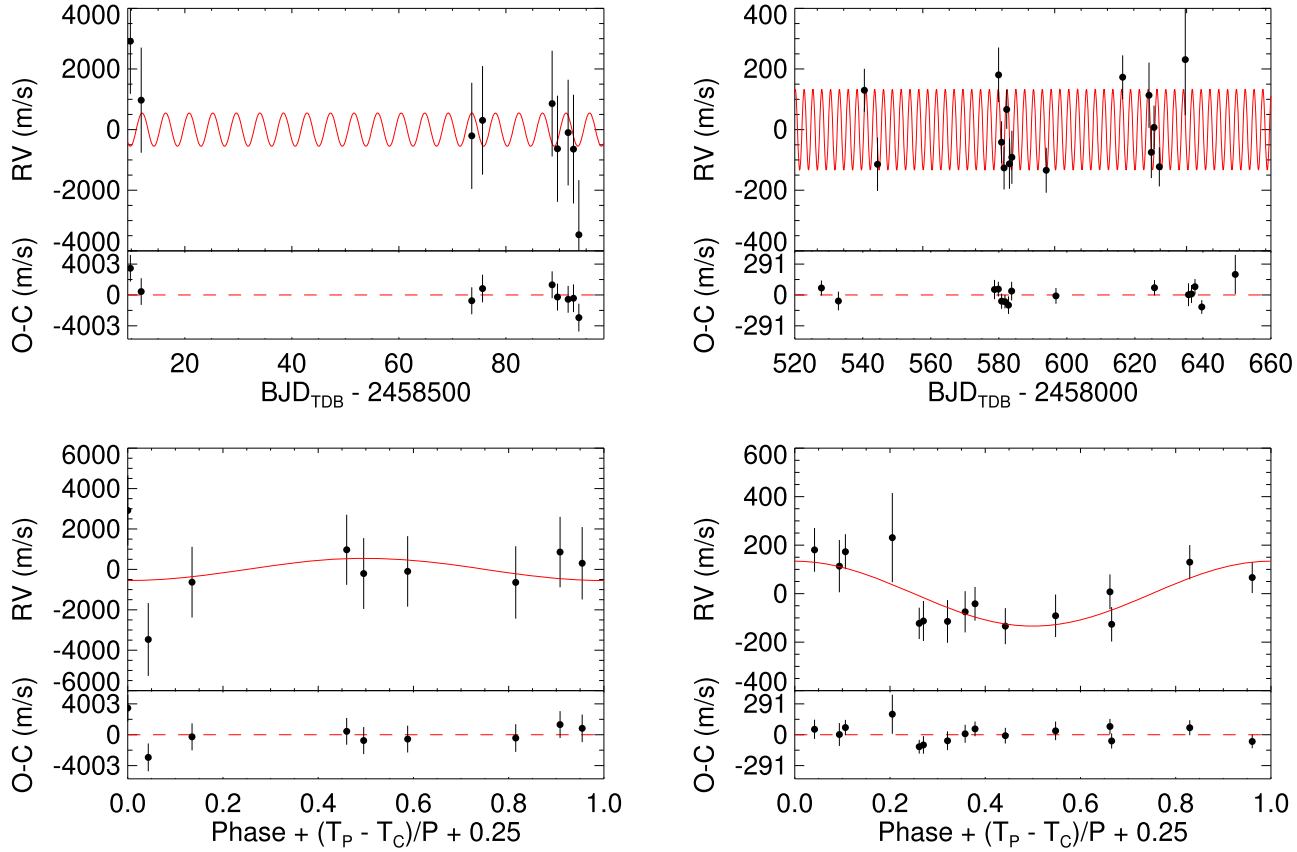

Figure 6. (Top) The relative RV measurements for KELT-25 b from TRES (left) and KELT-26 b from CHIRON (right). (Bottom) The RV measurements are phase-folded to the best determined period by EXOFASTv2. Here T_P is the time of periastron, while T_C is the time of conjunction or transit. Typically, the phases are referenced relative to the time of periastron; however, here they have been shifted such that the transit center is at phase 0.25. This is because this phase coincides with the RM signal, which was fit for in our models. Because of the fast rotation of KELT-25, EXOFASTv2 derives a negative mass for KELT-25 b (see Section 3.1). The RV phase-folded plot is therefore explicitly nonphysical (and hence why it looks inverted relative to that of KELT-26), with the primary transit at the time the RV model implies the planet is behind the star. This is intentional to avoid biasing the mass measurement high, but it is definitely nonintuitive. See an in-depth discussion of this in Section 9 of Eastman et al. (2019). The EXOFASTv2 model is shown in red, and the residuals to the best fit are shown below each plot.

Table 4
Relative Out-of-transit RVs for KELT-26 from CHIRON

BJD_{TDB}	RV (m s^{-1})	σ_{RV} (m s^{-1})
2,458,527.84082	132.1	54
2,458,532.82920	−112.1	75
2,458,578.72286	182.9	78
2,458,579.85037	−39.4	53
2,458,580.80996	−124	55
2,458,581.79719	68.9	45
2,458,582.83253	−110.5	69
2,458,583.76093	−89	75
2,458,596.78738	−131.7	59
2,458,625.76755	175.2	56
2,458,635.75959	115.8	97
2,458,636.64304	−72.5	72
2,458,637.66033	9.7	56
2,458,639.66539	−120.3	46
2,458,649.51090	233.2	180

determined by Bovy (2017) and thus is notable but not completely unexpected.

Both KELT-25 and KELT-26 have roughly the same galactocentric distance from the Sun. Assuming that the distance from the Sun to the Galactic center is roughly $R_0 = 8.2 \simeq$ kpc (Gravity Collaboration et al. 2019), we estimate galactocentric distances of 8.4 and 7.8 kpc for KELT-25 and KELT-26, respectively.

6. EXOFASTv2 Global Fits for KELT-25 and KELT-26

To constrain the system parameters, we modeled the available RVs, transit photometry, and multiband absolute photometry for KELT-25 and KELT-26 using the exoplanet-fitting software EXOFASTv2 (Eastman et al. 2013, 2019; Eastman 2017). EXOFASTv2 is a public exoplanet-fitting suite written in IDL. It allows individual as well as simultaneous modeling of different data sets, including multiple transits, RVs, and DT observations using a differential evolution Markov Chain Monte Carlo.

For each system, we globally fit the RVs (see Section 3), the TESS and follow-up photometry (see Sections 2.2 and 2.3), and the Doppler tomographic shadows simultaneously (see Sections 3.2–3.4). Within these fits, we determined the host star properties using a combination of spectroscopic priors, the spectral energy distribution, and the MESA Isochrones and Stellar Tracks (MIST) stellar evolution models (Paxton et al. 2011, 2013, 2015; Choi et al. 2016; Dotter 2016). For each system, we placed Gaussian priors of [Fe/H] $= 0.0 \pm 0.5$ dex for the metallicity of the host stars, as we did not have reliable constraints from our available spectra. From an independent EXOFASTv2 analysis of the KELT photometry, we adopted a Gaussian prior on the period of KELT-25 b of 4.401093 ± 0.000073 days and on

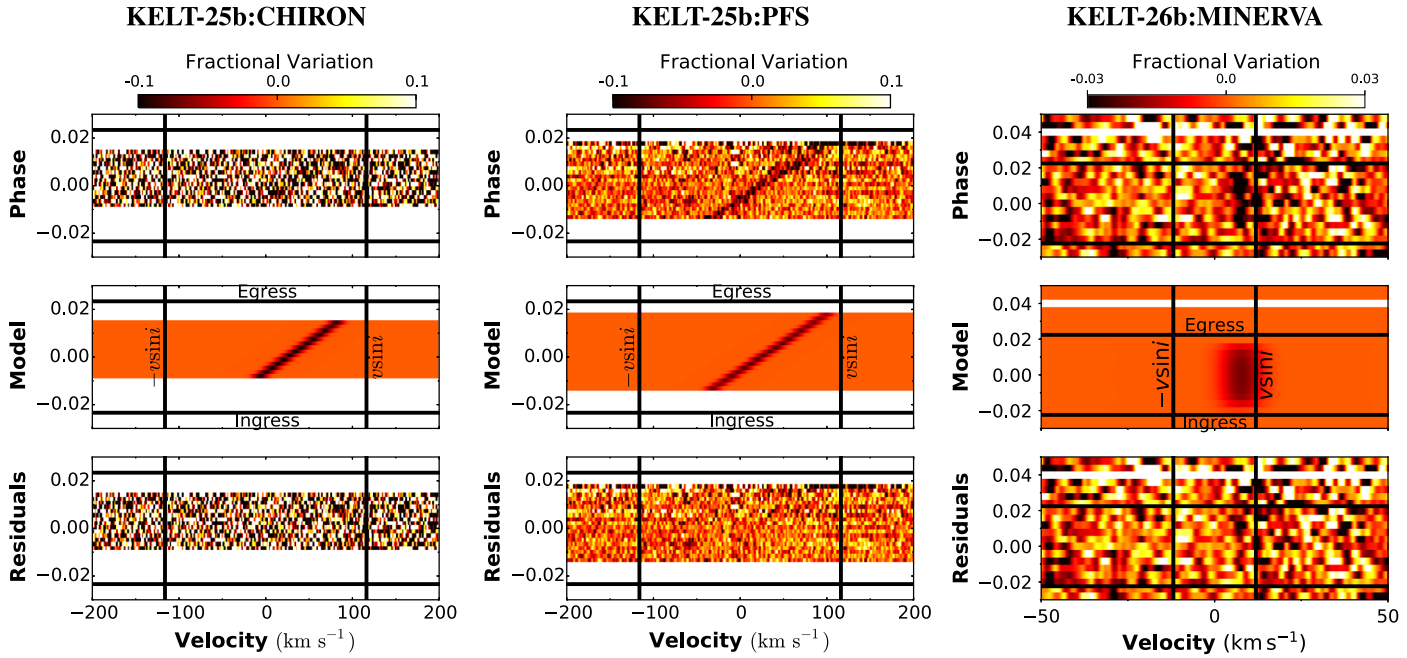

Figure 7. Spectroscopic transit signals of KELT-25 from CHIRON (left) and PFS (middle) and KELT-26 from MINERVA-Australis (right). The spectroscopic transit signal shown for KELT-26 from MINERVA-Australis is the combined signal from two telescopes (see Section 3.4). In the top panels, the shadow cast by the planet appears as a dark trail on the line profile residuals. The horizontal axis plots the velocity space of the line profile, while the vertical axis plots the phase, with positive phase increasing upward. The limits of stellar rotation are marked by the vertical lines, whereas the beginning and end of each transit are shown with the horizontal lines. The middle panel shows the best-fit model of the spectroscopic transit. The bottom panel shows the residuals after removal of the best-fit model, showing a general lack of correlated noise in the line profile subtractions, leading to higher confidence in the detection and a lack of any observable stellar surface oscillations.

the epoch of $T_c = 2{,}458{,}493.3144 \pm 0.00037$ BJD$_{\rm TDB}$. Similarly, we placed a Gaussian prior on the orbital period ($P = 3.344886 \pm 0.000064$ days) and the epoch ($T_c = 2{,}457{,}482.315 \pm 0.008600$ BJD$_{\rm TDB}$) of KELT-26 b. We also placed priors on the $v \sin I_*$ from spectroscopy for KELT-25 ($v \sin I_* = 111.277 \pm 1.422$ km s^{-1}) and KELT-26 ($v \sin I_* = 9.9349 \pm 1.1333$ km s^{-1}) and used parallaxes from Gaia DR2 (see Table 1). In addition, we assumed a circular orbit for both systems and fit for the depth of the secondary eclipse of KELT-25, observed in the bottom right panel of Figure 2. We constrained A_V to the maximum permitted line-of-sight extinction from Schlegel et al. (1998) and the temperature and stellar mass and radius from the SED best-fit values (see Figure 11 for the empirical SEDs of both systems). The best-fitting evolutionary models are shown in Figure 12, and the final fit parameters of the EXOFASTv2 analyses for both stars and their companions are shown in Tables 5–7.

Although a global fit to the photometry, RVs (including the DT measurements), and SED can completely constrain the properties of the system, we also include constraints from the MIST stellar evolutionary models, which include reasonably well-understood stellar physics, in our global fit. In this manner, we derive best-fit distances to both stars that are slightly different than those inferred from the Gaia parallaxes alone. As a result, we find a posterior distribution of the distance of KELT-25 after the global fit of $422.5^{+7.6}_{-7.3}$ pc, which is $\sim 0.6\sigma$ from that inferred from the Gaia parallax (see Table 1). Similarly, for KELT-26, we derive a posterior distance after the global fit of 417 ± 11 pc, which is $\sim 0.06\sigma$ from the distance inferred from the Gaia DR2 parallax alone. We consider these differences to be completely consistent within the uncertainties. To calculate the location of KELT-25 and KELT-26 within the Galaxy and their *UVW* space velocities in Section 5.1, we opted to use the model-independent parallaxes and distances from Gaia DR2. Although in this case, these distance measurements are completely consistent, the discovery of larger discrepancies in the fits of other systems may have implications for the current stellar evolutionary models or Gaia data. Thus, the empirical distances from Gaia DR2 can serve as a way to test and calibrate the models we use to derive fundamental stellar parameters or uncover evidence of systematic errors in the Gaia data themselves.

7. Discussion

Both KELT-25 b and KELT-26 b represent extreme transiting systems in a few key aspects. First, KELT-25 b and KELT-26 b both orbit relatively bright ($V \sim 10$ mag) and extremely hot ($T_{\rm eff} \simeq 8300$ and $\simeq 8700$ K, respectively) hosts, and they also have short orbital periods ($P \sim 4.4$ and 3.3 days, respectively). Their proximity to their host stars and their stars' intrinsic luminosity mean that they receive extreme amounts of stellar radiation, particularly high-energy radiation, resulting in high equilibrium temperatures—assuming zero albedo and complete redistribution—of $T_{\rm eq} = 2306$ K (KELT-25 b) and $T_{\rm eq} = 2402$ K (KELT-26 b). Both KELT-25 b and KELT-26 b join the recently defined class of planets called ultrahot Jupiters, which, similar to the prototype WASP-33b (Collier Cameron et al. 2010), are primarily planets on short-period orbits around early A stars. They are thus among the hottest transiting exoplanets known. Indeed, the equilibrium temperatures (estimated assuming zero albedo and complete heat distribution) of these planets are commonly in excess of 2000 K, and it seems likely that their dayside temperatures would be markedly higher still (see Figure 13).

Our EXOFASTv2 models (Table 6) indicate that the radii of both planets are also significantly inflated ($R_p = 1.64$ and 1.94 $R_{\rm J}$). From an irradiation evolution analysis of these systems (see Section 7.3), we conclude that these objects

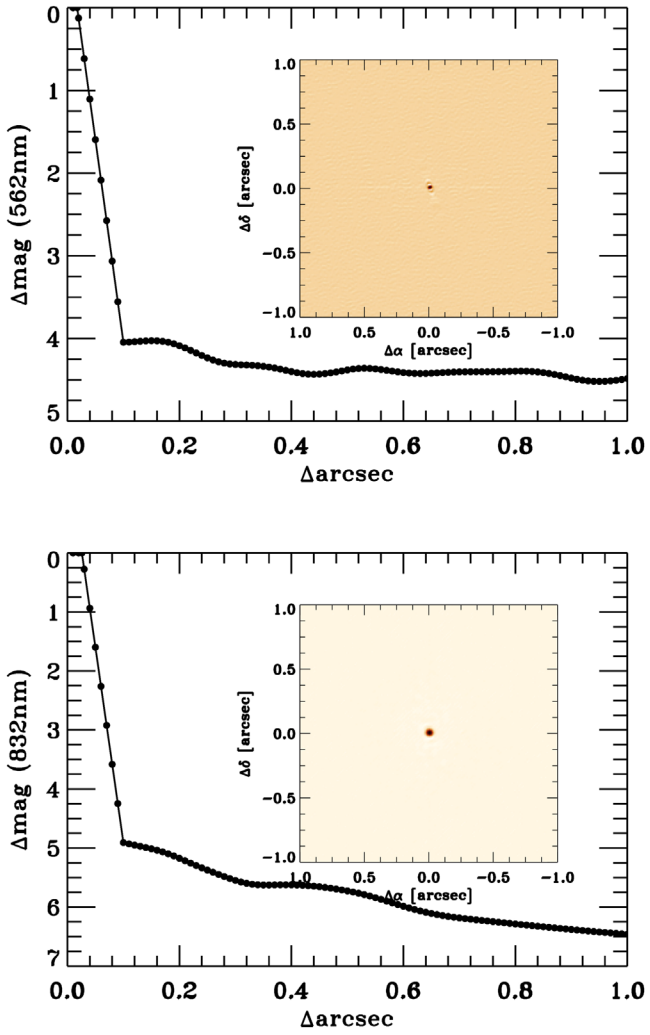

Figure 8. The 5σ contrast curves and 562 (inset, top) and 832 (inset, bottom) nm images for KELT-25 from the Zorro instrument from Gemini-South (N. Scott et al. 2019, in preparation).

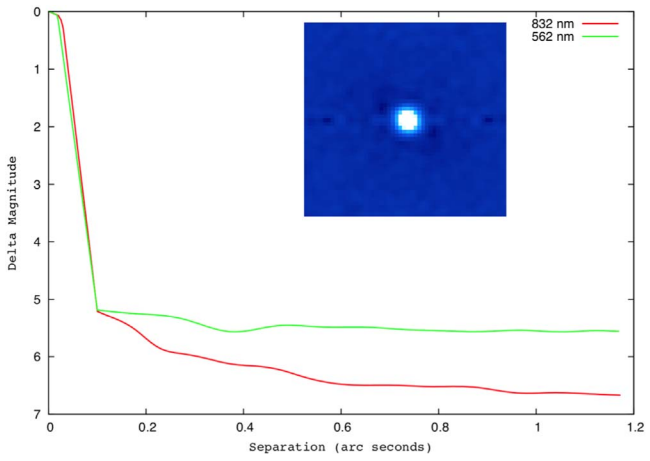

Figure 9. The 5σ contrast curves at 562 (green) and 832 (red) nm and image of KELT-26 from Gemini-South with the Zorro instrument.

currently receive an insolation flux of around 5×10^9 (KELT-25 b) and 1×10^{10} (KELT-26 b) erg s^{-1} cm^{-2}. Moreover, their orbital histories suggest that they have probably always been above the Demory & Seager (2011) insolation threshold

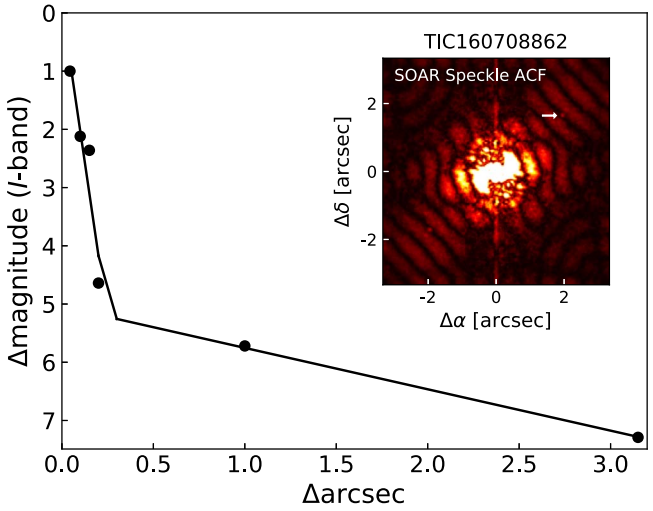

Figure 10. The I_c band ACF of the speckle image for KELT-26 from SOAR. The black points represent the 5σ sensitivity limits for KELT-26. The inset shows the ACF. A white arrow points to the location of the nearby companion. It is located $2\farcs4096$ away from the target at PA $= 311\fdg2$ and has a magnitude contrast of 7.1 mag in the I_c band. The companion is mirrored in the ACF on the opposite side due to the speckle processing.

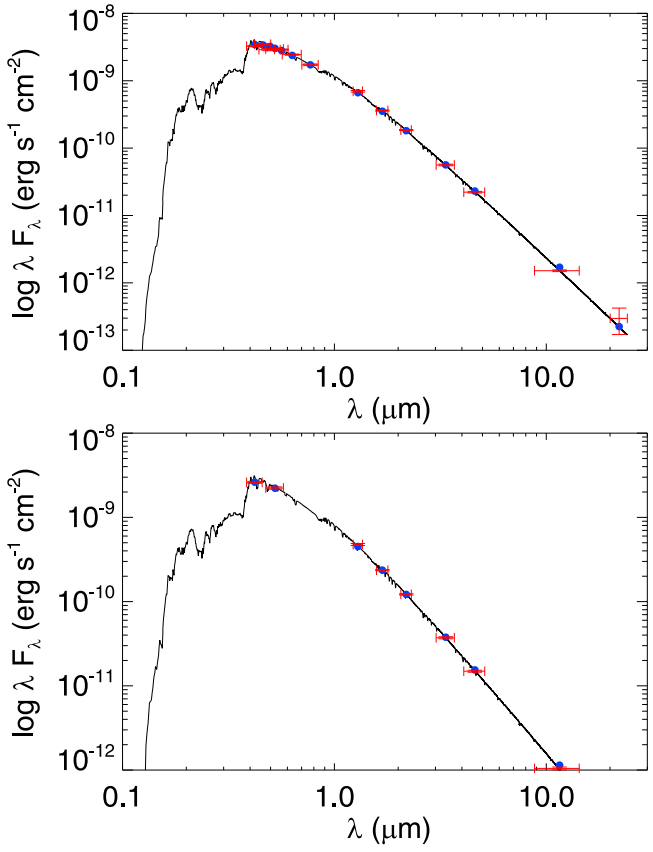

Figure 11. The SEDs for KELT-25 (top) and KELT-26 (bottom) from our EXOFASTv2 fits. The observed values are shown in red with 1σ uncertainties, while the predicted integrated fluxes are in blue. The final model is shown by the black line.

of 2×10^8 erg s^{-1} cm^{-2}, which is an empirical threshold above which giant planets exhibit significant radius inflation. For this reason, it is not surprising that they are both highly inflated. The extreme temperatures of these companions and the optical and infrared brightness of their hosts (KELT-25:

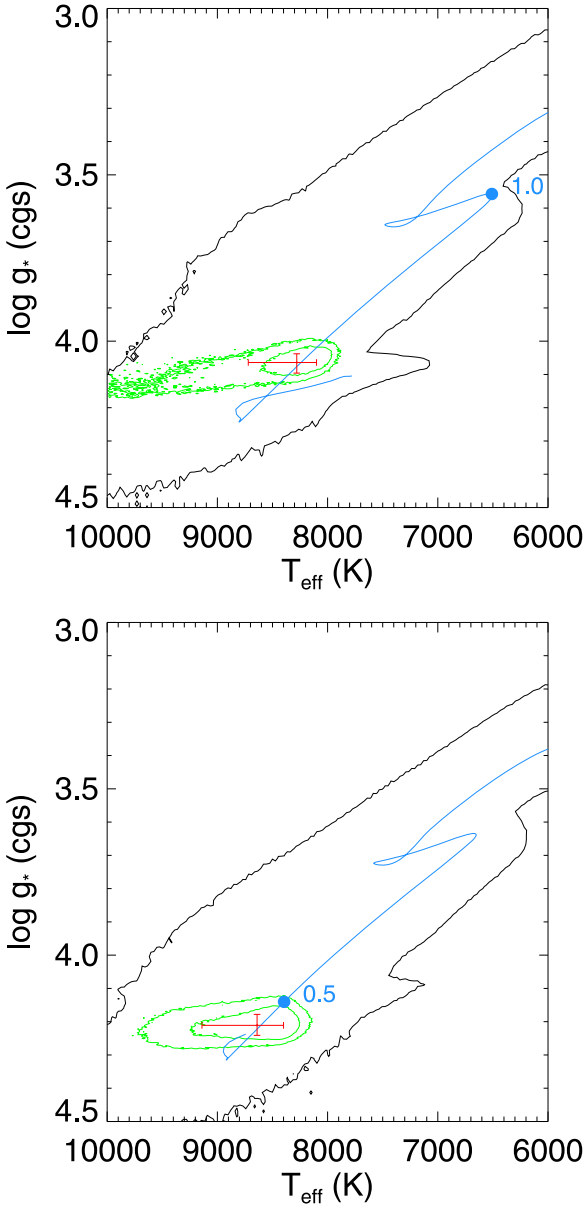

Figure 12. Best-fitting MIST track for KELT-25 (top) and KELT-26 (bottom), shown by the blue line. The black line shows the 3σ contours for the MIST evolutionary tracks. The red data point shows the median values and 1σ uncertainties from our global fit, while the green contours correspond to the 3σ errors. The blue points mark the location of 1.0 (top) and 0.5 (bottom) Gyr along the MIST track.

$V = 9.65$, $J = 9.36$; KELT-26: $V = 9.96$, $J = 9.77$ mag) mean that the prospects for detailed atmospheric characterization via transmission spectroscopy with the James Webb Space Telescope (JWST) or the Hubble Space Telescope (HST) are promising. Indeed, the TESS light curve for KELT-25 (Figure 2) demonstrates the weak but significant detection of the secondary eclipse of the system as the planet moves behind the star. Given the estimated equilibrium temperature of the star, this flux decrement is also certainly caused by the tail of the thermal emission from the planet. We estimate a secondary eclipse depth of $\sim$187 $\pm$ 46 ppm (see Table 7), implying a brightness temperature of the planet in the TESS band of $\sim 3396^{+140}_{-170}$ K, which is substantially higher than the equilibrium temperature (assuming zero albedo and complete heat redistribution) of 2303^{+100}_{-47} K.

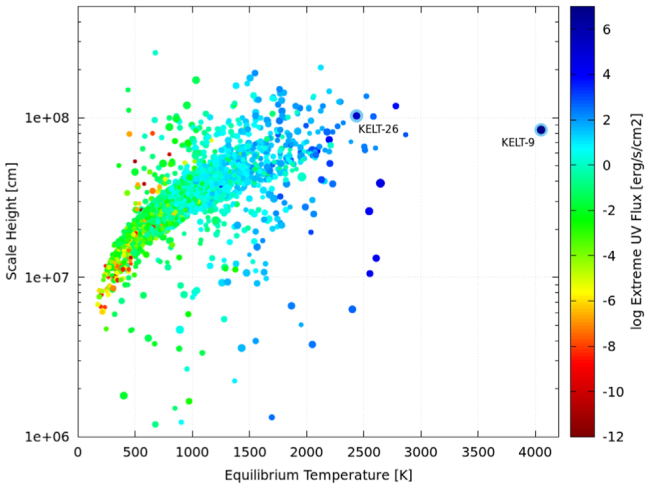

Figure 13. This scatter plot shows the atmospheric scale height vs. equilibrium temperature for all known transiting exoplanets with mass measurements. The color scale corresponds to the extreme ultraviolet radiation that planets receive from their host stars. The symbol sizes are inversely proportional to the magnitude in the V band of the host stars. At $T_{\rm eq} \sim 2402$ K, KELT-26 b stands out as one of the hottest known exoplanets, receiving extreme amounts of UV radiation, likely resulting in the exceptionally large radius of $R_p \sim 1.9\,R_{\rm J}$ and subsequently large scale height.

Table 5
Median Values and 68% Confidence Interval for the Stellar Parameters of KELT-25 and KELT-26 Derived from the Global Fit

Parameter	Description (Units)	Values KELT-25	Values KELT-26
M_*	Mass ($M_\odot$)	$2.18^{+0.12}_{-0.11}$	$1.93^{+0.14}_{-0.16}$
R_*	Radius ($R_\odot$)	$2.264^{+0.048}_{-0.052}$	$1.801^{+0.049}_{-0.048}$
L_*	Luminosity ($L_\odot$)	$21.8^{+4.6}_{-1.8}$	$16.4^{+3.8}_{-1.8}$
ρ_*	Density (cgs)	$0.263^{+0.025}_{-0.018}$	$0.463^{+0.040}_{-0.038}$
log g	Surface gravity (cgs)	$4.064^{+0.032}_{-0.026}$	$4.211^{+0.030}_{-0.033}$
$T_{\rm eff}$	Effective temperature (K)	8280^{+440}_{-180}	8640^{+500}_{-240}
[Fe/H]	Metallicity (dex)	$0.30^{+0.13}_{-0.21}$	$-0.06^{+0.30}_{-0.34}$
$[{\rm Fe/H}]_0$[a]	Initial metallicity	$0.34^{+0.11}_{-0.19}$	$0.03^{+0.25}_{-0.32}$
Age	Age (Gyr)	$0.46^{+0.14}_{-0.12}$	$0.43^{+0.31}_{-0.25}$
EEP[b]	Equal evolutionary phase	$342.0^{+6.3}_{-7.1}$	331^{+17}_{-28}
$v \sin I_*$	Projected rotational velocity (km s^{-1})	114.2 ± 1.2	$12.280^{+0.78}_{-0.82}$
$V_{\rm line}$[c]	Unbroadened line width (km s^{-1})	$3.7^{+2.3}_{-2.4}$	$6.4^{+1.8}_{-1.9}$
A_V	V-band extinction (mag)	$0.104^{+0.16}_{-0.073}$	$0.103^{+0.14}_{-0.078}$
$\sigma_{\rm SED}$	SED photometry error scaling	$2.50^{+0.78}_{-0.53}$	$1.76^{+0.81}_{-0.48}$
π	Parallax (mas)	$2.366^{+0.041}_{-0.042}$	2.396 ± 0.063
d	Distance (pc)	$422.7^{+7.6}_{-7.3}$	417 ± 11

Notes.
[a] The initial metallicity is the metallicity of the star when it was formed.
[b] The EEP corresponds to static points in a star's evolutionary history when using the MIST isochrones and can be a proxy for age. See Section 2 in Dotter (2016) for a more detailed description of EEP.
[c] The unbroadened line width is defined as the average line width without accounting for rotational broadening. This includes the effects of macroturbulence and thermal and pressure broadening (Eastman et al. 2019).

To better place these planets in the context of other known systems, we highlight KELT-26 b in Figure 13, which shows a plot of atmospheric scale height as a function of equilibrium temperature for all known transiting exoplanets with measured masses. KELT-26 b has a large scale height and receives

Table 6
Median Values and 68% Confidence Interval for the Physical Parameters of KELT-25 b and KELT-26 b from the Global Fit

Parameter	Description (Units)	Values KELT-25	Values KELT-26
P	Period (days)	4.401131 ± 0.000059	3.3448412 ± 0.0000033
R_P	Radius (R_J)	$1.642^{+0.039}_{-0.043}$	$1.940^{+0.060}_{-0.058}$
M_P	Mass (M_J)	(<64)	$1.41^{+0.43}_{-0.51}$
T_C	Time of conjunction (BJD_{TDB})	$2{,}458{,}493.31501 \pm 0.00037$	$2457482.31209^{+0.00090}_{-0.00091}$
T_0[a]	Optimal conjunction time (BJD_{TDB})	$2{,}458{,}506.51840 \pm 0.00034$	$2458321.86724^{+0.00038}_{-0.00039}$
a	Semimajor axis (au)	$0.0681^{+0.0012}_{-0.0011}$	$0.0545^{+0.0013}_{-0.0015}$
i	Inclination (deg)	$85.37^{+0.55}_{-0.42}$	$84.45^{+0.39}_{-0.41}$
T_{eq}	Equilibrium temperature (K)	2306^{+100}_{-47}	2402^{+130}_{-71}
K	RV semiamplitude (m s^{-1})	(<4687.8)	123^{+37}_{-45}
$\log K$	Log of RV semiamplitude	(<3.64)	$2.09^{+0.11}_{-0.20}$
R_P/R_*	Radius of planet in stellar radii	$0.07450^{+0.00039}_{-0.00042}$	$0.11066^{+0.00090}_{-0.00087}$
a/R_*	Semimajor axis in stellar radii	$6.46^{+0.20}_{-0.15}$	6.49 ± 0.18
δ	Transit depth (fraction)	$0.005550^{+0.000059}_{-0.000062}$	$0.01225^{+0.00020}_{-0.00019}$
τ	Ingress/egress transit duration (days)	$0.0192^{+0.0011}_{-0.0012}$	$0.0238^{+0.0016}_{-0.0014}$
T_{14}	Total transit duration (days)	$0.2051^{+0.0013}_{-0.0015}$	0.1514 ± 0.0016
T_{FWHM}	FWHM transit duration (days)	$0.18586^{+0.00097}_{-0.00096}$	$0.12760^{+0.00098}_{-0.00099}$
b	Transit impact parameter	$0.522^{+0.034}_{-0.048}$	$0.628^{+0.027}_{-0.029}$
$\delta_{S,3.6\,\mu m}$	Blackbody eclipse depth at 3.6 μm (ppm)	732^{+27}_{-23}	1664^{+82}_{-72}
$\delta_{S,4.5\,\mu m}$	Blackbody eclipse depth at 4.5 μm (ppm)	872^{+26}_{-24}	1965^{+83}_{-74}
ρ_P	Density (cgs)	(<18.3)	$0.238^{+0.077}_{-0.088}$
$\log g_P$	Surface gravity	(<4.77)	$2.97^{+0.12}_{-0.20}$
λ	Projected spin–orbit alignment (deg)	$23.4^{+3.2}_{-2.3}$	$91.3^{+6.5}_{-6.3}$
Θ	Safronov number	$-0.01^{+0.50}_{-0.48}$	$0.041^{+0.012}_{-0.015}$
$\langle F \rangle$	Incident flux (10^9 erg s^{-1} cm^{-2})	$6.42^{+1.2}_{-0.51}$	$7.56^{+1.7}_{-0.86}$
T_S	Time of eclipse (BJD_{TDB})	$2{,}458{,}495.51558 \pm 0.00036$	$2{,}457{,}483.98451 \pm 0.00090$
T_A	Time of ascending node (BJD_{TDB})	$2{,}458{,}496.61586 \pm 0.00035$	$2{,}457{,}484.82072 \pm 0.00090$
T_D	Time of descending node (BJD_{TDB})	$2{,}458{,}494.41530 \pm 0.00036$	$2{,}457{,}483.14830 \pm 0.00090$
$M_P \sin i$	Minimum mass (M_J)	(<64)	$1.40^{+0.43}_{-0.51}$
M_P/M_*	Mass ratio	(<0.028)	$0.00070^{+0.00021}_{-0.00026}$
d/R_*	Separation at mid-transit	$6.46^{+0.20}_{-0.15}$	6.49 ± 0.18
P_T	A priori nongrazing transit prob.	$0.1433^{+0.0035}_{-0.0043}$	$0.1370^{+0.0039}_{-0.0036}$
$P_{T,G}$	A priori transit prob.	$0.1664^{+0.0041}_{-0.0051}$	$0.1710^{+0.0050}_{-0.0047}$
Telescope Parameters		TRES	CHIRON
γ_{rel}	Relative RV offset (m s^{-1})	720^{+810}_{-820}	-25595^{+25}_{-24}
σ_J	RV jitter (m s^{-1})	2240^{+1100}_{-620}	67^{+32}_{-23}

Note.
[a] Minimum covariance with period. All values in this table for the secondary occultation of KELT-25 b are predicted values from our global analysis. All values in red are 3σ upper limits on mass-dependent parameters for KELT-25 b. The eccentricity was fixed to zero for both KELT-25 b and KELT-26 b.

extreme amounts of UV radiation from its host. Figures 14 and 15 show the distributions of $v \sin I_*$ and spin–orbit misalignments λ versus stellar temperature for A stars ($v \sin I_*$ distribution) of all known planet hosts with measured spin–orbit angles.

With KELT-25 b and KELT-26 b, we have a large enough sample of A stars with transiting exoplanets that we can begin to see emerging patterns in the population (see Table 8). All of the confirmed planets around A stars have short periods (1.22 days $< P <$ 4.79 days) and transit bright host stars ($V \lesssim 10$), which, as previously remarked, makes them attractive targets for atmospheric characterization with the upcoming JWST. Before JWST launches, however, TESS may be able to observe these planets in transit, in some cases even resolving their secondary eclipses, as with KELT-25 b. These observations can constrain the brightness temperature of these planets and therefore provide insights into the heat distribution mechanisms of their atmospheres.

7.1. KELT-26 b: A Giant Planet Orbiting a Likely Am Star with a Likely Significant Transit Asymmetry

KELT-26 b orbits a relatively young (~430 Myr), slowly rotating A star ($v \sin I_* = 12.2$ km s^{-1}). This rotational velocity is rather atypical for an early A star, as such stars tend to be much faster rotators, on average. From the Doppler tomographic observations (see Section 3), we also measured the projected spin–orbit angle of this system and concluded that it is on an orbit that is consistent with being exactly perpendicular to the projected stellar equator, with $\lambda = 91.3^{+6.5}_{-6.3}$. The projected spin–orbit alignment λ need not be the true obliquity ψ, which is a more fundamental quantity of the system. However, the latter is harder to constrain, as explained in

Table 7
Median Values and 68% Confidence Interval for Global Model of KELT-25 and KELT-26 from the Global Fit

KELT-25 b				
Wavelength Parameters		R	TESS	
u_1	Linear limb-darkening coeff.	0.292 ± 0.049	0.159 ± 0.029	
u_2	Quadratic limb-darkening coeff.	0.348 ± 0.049	0.260 ± 0.035	
A_T	Secondary eclipse depth (ppm)		187 ± 46	
Transit Parameters		PEST UT 2019-01-18 (R)	TESS Sector 7	TESS Sector 7 (secondary)
σ^2	Added variance	$0.00000779^{+0.00000062}_{-0.00000058}$	$-0.0000000863^{+0.0000000057}_{-0.0000000050}$	$-0.0000000885^{+0.0000000066}_{-0.0000000057}$
F_0	Baseline flux	1.00362 ± 0.00013	0.999826 ± 0.000049	0.999811 ± 0.000040
DT Parameters				
$\sigma_{\rm DT}$	DT error scaling	$0.9975^{+0.0100}_{-0.0098}$	$0.9839^{+0.0057}_{-0.0056}$	
KELT-26 b				
Wavelength Parameters		I	r'	TESS
u_1	Linear limb-darkening coeff.	0.185 ± 0.048	0.207 ± 0.045	0.212 ± 0.044
u_2	Quadratic limb-darkening coeff.	0.264 ± 0.051	0.279 ± 0.048	0.280 ± 0.047
Transit Parameters		PEST UT 2016-07-26 (I)	CDK700 UT 2018-03-20 (r')	TESS UT 2019-04-07 (TESS)
σ^2	Added variance	$0.00000780^{+0.0000010}_{-0.00000089}$	$0.00000170^{+0.00000025}_{-0.00000021}$	$0.000000420^{+0.000000029}_{-0.000000027}$
F_0	Baseline flux	0.99573 ± 0.00021	0.99891 ± 0.00015	1.000000 ± 0.000026
DT Parameters		MINERVA 3	MINERVA 4	
$\sigma_{\rm DT}$	DT error scaling	0.991 ± 0.013	0.997 ± 0.012	

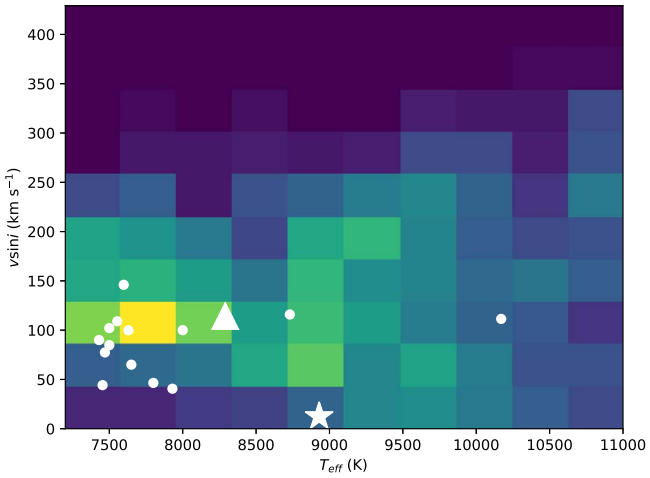

Figure 14. Distribution of rotational velocities in units of km s^{-1} as a function of stellar effective temperature for all of the measured A-type planet hosts in the literature. The color scale is proportional to the fraction of A stars at that effective temperature that lie within each bin; warmer colors indicate a higher fraction of A stars. The sample is from Zorec & Royer (2012). The big triangle and star represent KELT-25 and KELT-26, respectively. KELT-26 displays an unusually slow rotation for its temperature, which could be the result of the orientation of its spin axis along our line of sight rather than an intrinsic slow rotation.

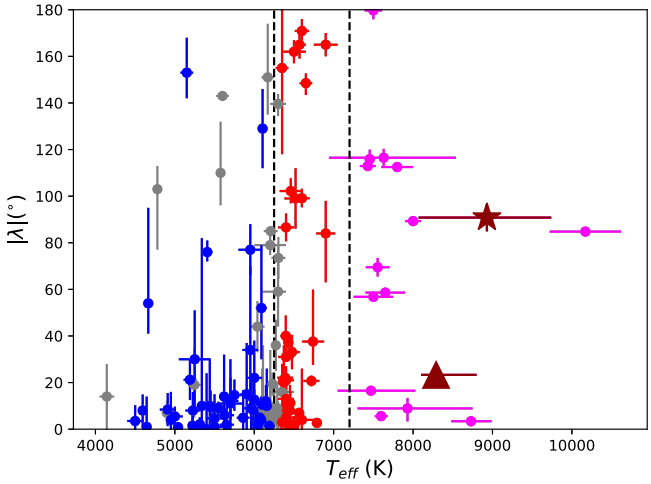

Figure 15. Distribution of projected spin–orbit misalignments λ as a function of stellar effective temperature for all of the measured hot Jupiters in the literature (the format of this plot is derived from Winn 2010). Planets around cool stars ($T_{\rm eff} < 6250$ K) are represented by blue dots; the red dots represent hot stars ($T_{\rm eff} > 6250$ K), while those with uncertainties in $\lambda > 20°$ are gray. The dashed vertical lines mark the location of the Kraft break (left) and the approximate dividing line between F and A spectral types. The A stars are shown in magenta. The crimson star and triangle depict KELT-26 b and KELT-25 b, respectively. The literature sample was taken from John Southworth's TEPCat RM catalog (https://www.astro.keele.ac.uk/jkt/tepcat/).

Johnson et al. (2018), because it requires knowledge of both the planetary orbital inclination i and the stellar spin axis I_*. The observation of an orbit that has $\lambda \sim 90°$ with the unusually slow rotation period of KELT-26 ($v \sin I_* = 12.2$ km s^{-1}) may imply that the star is perhaps spinning faster but we are observing it nearly pole-on. The phase-folded TESS light curve of the primary (Figure 3) appears to show a slight asymmetry, such that the planet is first passing over a region of the star with higher-than-average surface brightness, whereas the planet later passes over a region of the star with lower surface brightness. This would be expected from gravity darkening, assuming the planet first passes over or near the pole and then over the lower surface brightness equator (Barnes 2009). Gravity darkening has already been observed with TESS for two hot Jupiters, HAT-P-69 b (TOI 625.01) and HAT-P-70 b (TOI 624.01; Zhou et al. 2019b), and is also clear in the unpublished TESS light curve of KELT-9 (Wong et al. 2020; J. Ahlers et al. 2020, in preparation; P. Wachiraphan et al. 2020, in preparation). However, as we discuss below, the host star KELT-26 also appears to be variable at the ∼few millimagnitude level at a period that is nearly commensurate (1:18) with the period of the

Table 8
A Star Transiting Planet Hosts from the Literature Ordered by Decreasing Stellar Temperature

Planet	M_p (M_J)	R_p (R_J)	$T_{\rm eff}$ (K)	P (days)	$L_\star$ ($L_\odot$)	$T_{\rm eq}$ (K)	λ (deg)	SpT	References
KELT-9 b	2.88 ± 0.84	$1.891^{+0.061}_{-0.053}$	10170 ± 450	1.48	53^{+13}_{-10}	4050 ± 180	-84.8 ± 1.4	A0	1
KELT-20 b/ MASCARA-2 b	<3.5 (3σ)	$1.735^{+0.07}_{-0.075}$	8730^{+250}_{-260}	3.47	$12.7^{+2.2}_{-1.9}$	$\sim$2250	3.4 ± 2.1	A2	2
KELT-26 b	$1.41^{+0.43}_{-0.51}$	$1.940^{+0.060}_{-0.058}$	8640^{+500}_{-240}	3.34	$16.4^{+3.8}_{-1.8}$	2402^{+130}_{-71}	$91.3^{+6.5}_{-6.3}$	A3m	3
HAT-P-70 b	<6.14	$2.011^{+0.051}_{-0.114}$	8450^{+540}_{-690}	2.74	$16.7^{+5.3}_{-4.6}$	2562^{+43}_{-52}	$116.5^{+3.5}_{-3.8}$	A3V	4
KELT-25 b	<64	$1.642^{+0.039}_{-0.043}$	8280^{+440}_{-180}	4.40	$21.8^{+4.6}_{-1.8}$	2306^{+100}_{-47}	$23.4^{+3.2}_{-2.3}$	A4	5
WASP-189 b	2.13 ± 0.28	1.374 ± 0.082	8000 ± 100	2.72	1.293 ± 0.045	2641 ± 34	89.3 ± 1.4	A6IV-V	6
HATS-70 b	$12.9^{+1.8}_{-1.6}$	$1.384^{+0.079}_{-0.074}$	7930^{+630}_{-820}	1.89	$12.0^{+5.5}_{-3.4}$	2730^{+140}_{-160}	$8.9^{+5.6}_{-4.5}$	A6V	7
MASCARA-4 b	3.1 ± 0.9	$1.53^{+0.07}_{-0.04}$	7800 ± 200	2.82	12.23 ± 0.655	2100 ± 100	$247.5^{+1.5}_{-1.7}$	A7V	8
Kepler-13A b	$\sim 9.2 \pm 1.1$	1.512 ± 0.035	7650 ± 250	1.76	...	2550 ± 80	58.6 ± 2.0	A8V	9
KELT-21 b	<3.91 (3σ)	$1.586^{+0.039}_{-0.040}$	7598^{+81}_{-84}	3.61	$8.03^{+0.54}_{-0.53}$	2051^{+29}_{-30}	$-5.6^{+1.7}_{-1.9}$	A8V	10
MASCARA-1 b	3.7 ± 0.9	1.5 ± 0.3	7554 ± 150	2.14	13.1 ± 3	2570^{+50}_{-30}	69.5 ± 3	A8V	11
HAT-P-57 b	1.41 ± 1.52	1.74 ± 0.36	7500 ± 250	2.46	6.4 ± 1.1	2200	-16.7-3.3 or 2.76-57.4	A8V	12
KELT-19A b	$1.62^{+0.25}_{-0.20}$	1.83 ± 0.10	7500 ± 110	4.61	$9.5^{+1.2}_{-1.1}$	$\sim$1935	$-179.7^{+3.7}_{-3.8}$	Am	13
KELT-17 b	$1.31^{+0.28}_{-0.29}$	$1.525^{+0.065}_{-0.060}$	7454 ± 49	3.08	$7.51^{+0.62}_{-0.55}$	2087^{+32}_{-33}	-115.9 $\pm$ 4.1	A9V	14
WASP-33 b	4.1	1.497 ± 0.045	7430 ± 100	1.22	...	2710 ± 50	251.6 ± 0.7	A9V	15
HAT-P-69 b	$3.54^{+0.61}_{-0.60}$	1.714 ± 0.028	7394^{+360}_{-600}	4.79	$10.0^{+1.8}_{-0.9}$	1930^{+80}_{-230}	$16.5^{+2.1}_{-1.9}$	A9V	16

References. (1) Gaudi et al. (2017), (2) Lund et al. (2017), Talens et al. (2018), (3) this work, (4) Zhou et al. (2019b), (5) this work, (6) Anderson et al. (2018), (7) Zhou et al. (2019b), (8) Dorval et al. (2020), (9) Esteves et al. (2015), Johnson et al. (2014), (10) Johnson et al. (2018), (11) Talens et al. (2017), (12) Hartman et al. (2015), (13) Siverd et al. (2018), (14) Zhou et al. (2016), (15) Collier Cameron et al. (2010), (16) Zhou et al. (2019a).

planet. This variability may also be causing the slight asymmetry.

A Lomb–Scargle periodogram (Lomb 1976; Scargle 1982) of the TESS light curve of KELT-26 shows a significant peak at a period of 0.185 days with an amplitude of 0.115%, or 1.25 mmag. This period is nearly 1/18 (1/18.06, to be precise) of the period of the planet. We do not know if this is simply a coincidence, as the mass of the companion is likely too small to induce periodic oscillations on its host star. Both KELT-25 and KELT-26 are inside the instability strip, where one might expect to find δ Scuti pulsations. Indeed, the period and amplitude of the variability of KELT-26 are consistent with other δ Scuti variables. A more detailed study of the nature of the intrinsic variability of KELT-26 is beyond the scope of this paper.

On the other hand, the spectrum of KELT-26 shows evidence of being an Am star (or "metallic-line A star"). The Am stars typically rotate much more slowly than A stars of the same effective temperature. This is usually attributed to a stellar companion that has spun down the star or otherwise "stolen" its angular momentum at birth. However, we find no evidence of a stellar companion that would affect the spin rate of KELT-26, and the planetary companion is not sufficiently massive to play this role. The Am stars are typically identified by the fact that the star does not appear to have a consistent metallicity when measured using absorption lines formed at different depths in the photosphere. This can be seen in Figure 16, where it is clear that for models with a fixed $T_{\rm eff}$ and varying [Fe/H], no single model can simultaneously fit all of the spectral lines.

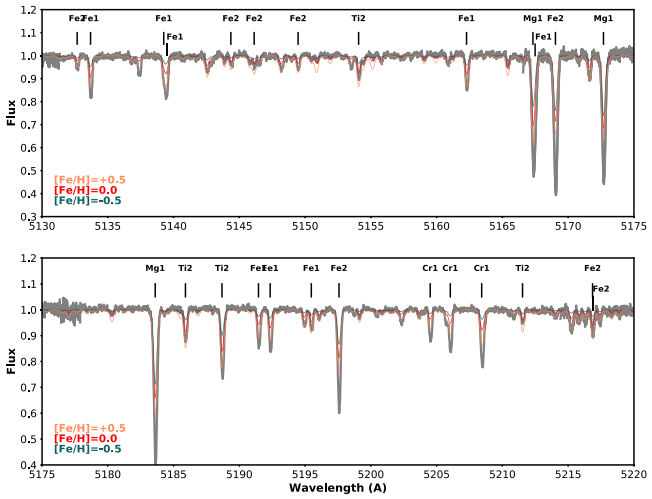

Figure 16. A portion of the CHIRON spectrum near the Mg b region for KELT-26 is shown in gray. The other lines show a set of $T_{\rm eff} = 9000$ K, $\log g_\star = 4.25$ synthetic spectra with [Fe/H] of -0.5 (green), 0.0 (red), and $+0.5$ (orange) dex, generated with the ATLAS9 model atmospheres (Castelli & Kurucz 2003), demonstrating that a single [Fe/H] cannot simultaneously fit all of the observed spectral features.

7.2. KELT-25 b: A Substellar Object Transiting a Rapidly Rotating Young A Star and Likely Cluster Member

With a $v \sin I_*$ of 114.2 km s^{-1}, KELT-25 is rotating much faster than KELT-26, and this has implications for the dynamical history of its potential planet. In this case, the classical scenario of hot Jupiters spiraling toward their host stars is reversed. The stellar tidal dissipation causes the semimajor axis of KELT-25 b's orbit to gradually increase (see Section 7.3). As a result, KELT-25 b will avoid getting engulfed by its host star, at least until the star leaves the main sequence. The DT shadows (Figure 7) suggest that it is on a prograde aligned orbit ($\lambda = 23.4^{+3.2}_{-2.3}$). To estimate the age of the systems, we show a modified Hertzsprung–Russell diagram ($\log g_*$ versus $T_{\rm eff}$) in Figure 12. From the MIST stellar evolutionary models, and taking the 1σ upper limit on the mass for KELT-25, we infer an age of $0.46^{+0.14}_{-0.12}$ Gyr. Using the same models, we obtain an age for KELT-26 of $0.43^{+0.31}_{-0.25}$ Gyr.

7.2.1. Is KELT-25 a Member of a Stellar Cluster, Association, or Moving Group?

We cross-matched existing TESS objects of interest (TOIs) to the catalog of clusters presented in Kounkel & Covey (2019), and we found a match between TOI-626.01 (KELT-25) and one of the putative clusters identified in that paper as Theia 449. In that paper, they identified 1900 clusters from an analysis of the distribution of sources in five-dimensional space (three-dimensional position and two-dimensional (e.g., transverse) velocity) in Gaia DR2. They then performed a clustering analysis on Gaia sources within $|b| < 30^{\circ}$ of the Galactic plane and parallaxes with $\pi > 1$ mas using a Python implementation of Hierarchical Density-Based Spatial Clustering of Applications with Noise (HDBSCAN; McInnes et al. 2017). They estimated the ages of their clusters and associations by applying a combination of machine-learning and isochronal-fitting techniques to determine the ages of their sources to a precision of ∼0.15 dex.

For the cluster Theia 449, Kounkel & Covey (2019) reported a mean Galactic latitude of $b = -7.^{\circ}13$, a mean parallax of 2.37 ± 0.82 mas, an age of 0.162 Gyr, and a mean RV of 23.54 ± 18.21 km s^{-1}. From our MIST models, we determine that KELT-25 is a young A star with an age of $0.46^{+0.14}_{-0.12}$ Gyr, which is just $\sim 2\sigma$ discrepant with the mean reported age of the cluster. Our derived properties for KELT-25 are thus in general agreement with the average properties of Theia 449. However, the broader issue of whether Theia 449 truly represents a collection of coeval stars is outside the scope of this paper. Clarification of the status of Theia 449 could help resolve the age, metallicity, and formation environment of KELT-25.

7.2.2. Is KELT-25 b a Planet or Brown Dwarf?

Given the extremely fast rotation of the host star, we were only able to constrain the mass of KELT-25 b to a 3σ upper limit of ∼64 M_J, or a 1σ upper limit of 5.46 M_J. We argue that KELT-25 b is likely to be a planet or low-mass brown dwarf based on several lines of reasoning. First, substellar companions at the upper end of the allowed mass range and with this period are known to be relatively rare (the so-called "brown dwarf desert"; e.g., Grether & Lineweaver 2006). Second, no brown dwarfs are known that are as highly inflated as KELT-25 b (Zhou et al. 2019a). Inspection of Figures 9 of Zhou et al. (2019a) and Šubjak et al. (2020) and Figure 11 of Carmichael et al. (2020) reveal that not only do no brown dwarfs have radii as large as KELT-25 b, only about a dozen lower-mass transiting planets have radii this large. Šubjak et al. (2020) argued that although brown dwarfs orbiting hot stars are expected to experience strong irradiative effects and therefore have slightly more inflated atmospheres than those orbiting cooler stars, this effect would be counteracted by the higher surface gravity resulting from the larger mass of the brown dwarf. Given the large surface gravity expected if KELT-25 b had a mass significantly above the deuterium-burning limit, this is strong circumstantial evidence that it is less massive. Finally, there is no evidence of Doppler beaming (Loeb & Gaudi 2003) or ellipsoidal variability (Drake 2003) in the KELT-25 b TESS light curve, which would likely be expected if KELT-25 b had a mass substantially above the deuterium-burning limit. The weight of evidence indicates that KELT-25 b is most likely a giant planet or very low mass brown dwarf.

7.2.3. Intrinsic Variability of KELT-25

As mentioned previously, both KELT-25 and KELT-26 are inside the instability strip. Only about 40% of stars within this range of $T_{\rm eff}$ show δ Scuti pulsations (Murphy et al. 2019; see their Figure 11). While KELT-26 does show variability consistent with δ Scuti pulsations (see Section 7.1), we find no evidence of intrinsic variability in the KELT-25 TESS light curve.

7.3. Tidal Evolution and Irradiation History

We estimated the orbital and irradiation evolution of KELT-25 and KELT-26; in particular, we calculated the history of the companions' semimajor axis and irradiation as a function of stellar age using the Planetary Orbital Evolution due to Tides (POET; Penev et al. 2014). POET assumes a constant tidal phase lag or quality factor $Q_\star$, a circular orbit, and no perturbations in the orbits due to unseen stellar or planetary companions. We further assumed that the tides raised by the planet or substellar companion are negligible and that the evolution of the planet's orbit is therefore dominated by the dissipation of tidal perturbations in the star (as explained in Rodriguez et al. 2019a). We accounted for the changes in stellar radius and luminosity in time by using a MIST stellar evolutionary track corresponding to the best-fit stellar properties (see Section 6). Because of the large uncertainties in the knowledge of the tidal dissipation in stars and the tidal quality factor, $Q_\star$, we consider different constant values of the dissipation parameter $Q'_\star$, namely, $Q'_\star = 10^{6.6}$, 10^7, and 10^8 for KELT-25 and $Q'_\star = 10^5$, 10^6, and 10^7 for KELT-26, where $Q'_\star$ is just proportional to $Q_\star$. With these assumptions, we proceeded to calculate the past and future evolution of the semimajor axis (in units of the stellar radius) as a function of the age of the systems.

For KELT-26 b, we can see in Figure 18 (top) that for every assumed dissipation parameter $Q'_\star$, the planet's orbit moderately decays until the present age of the system. Beyond that point, the future evolution of the planet's orbit strongly depends on $Q'_\star$: for $Q'_\star = 10^5$, the planet gradually falls into the star within 500 Myr. For higher values of $Q'_\star$, the planet would take longer to be engulfed by its host star, perhaps surviving the entire stellar lifetime. As a consequence of its decaying orbit, KELT-26 b's incident flux increases for all assumed dissipation parameters, as expected. We further note that KELT-26 b has remained subjected throughout its lifetime to radiation above the 2×10^8 erg s^{-1} cm^{-2} insolation threshold established in Demory & Seager (2011). This likely explains why KELT-26 b is presently significantly inflated, with $R_p = 1.9 R_J$.

In contrast to KELT-26, because KELT-25 is so rapidly rotating ($v \sin I_* = 114.2$ km s^{-1}) and the stellar rotation period is probably shorter than the companion's orbital period, the object's semimajor axis increases with time, rather than decreases, for all physical values of $Q'_\star$. The lowest value of $Q'_\star$ of $10^{6.6}$ predicts the fastest orbital evolution. If $Q'_\star$ is close to 10^8, the decreasing insolation due to the planet's expanding orbit will be offset by an increase in stellar radiation as the evolving host expands, resulting in a net increase in incident flux. For all of these calculations, the 3σ upper limit on the mass of KELT-25 b was assumed. Because we did not have the moment of inertia for KELT-25, we could not compute its rotational history, so all of the orbital paths were calculated

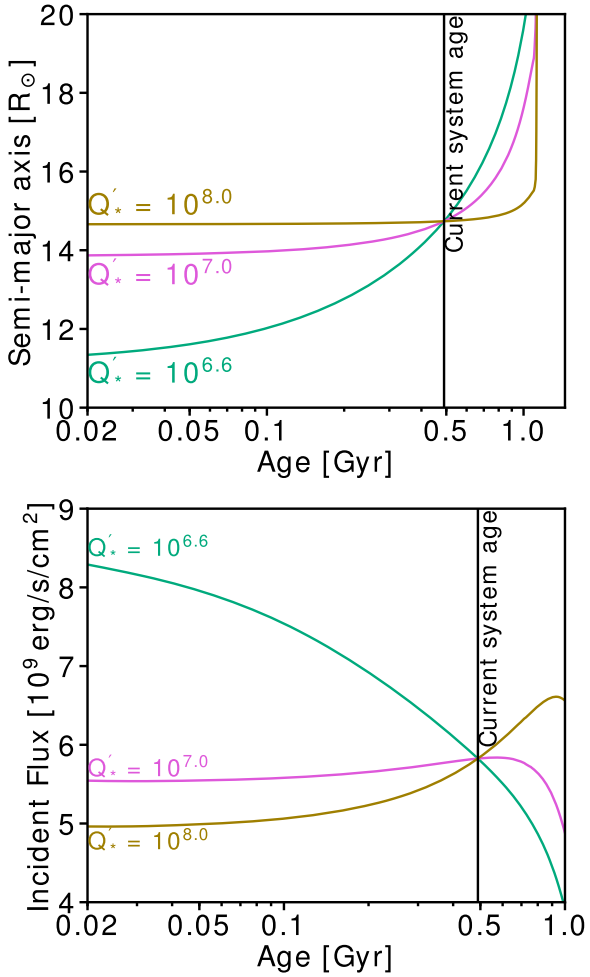

Figure 17. Evolution of the semimajor axis in units of stellar radius (top) and incident flux (stellar radiation) as a function of stellar age (bottom) of KELT-25 b for constant values of $Q_\star^{'}$ of $10^{6.6}$ (turquoise), 10^7 (pink), and 10^8 (gold). The semimajor axis seems to diverge at around 1 Gyr because at that time, the star begins to approach the end of its main sequence. This causes the radius to rapidly expand and increase the rate of tidal evolution. For any given dissipation parameter, the semimajor axis increases with time, while the incident flux increases for $Q_\star^{'} = 10^8$ and decreases for $Q_\star^{'} = 10^{6.6}$ and 10^7.

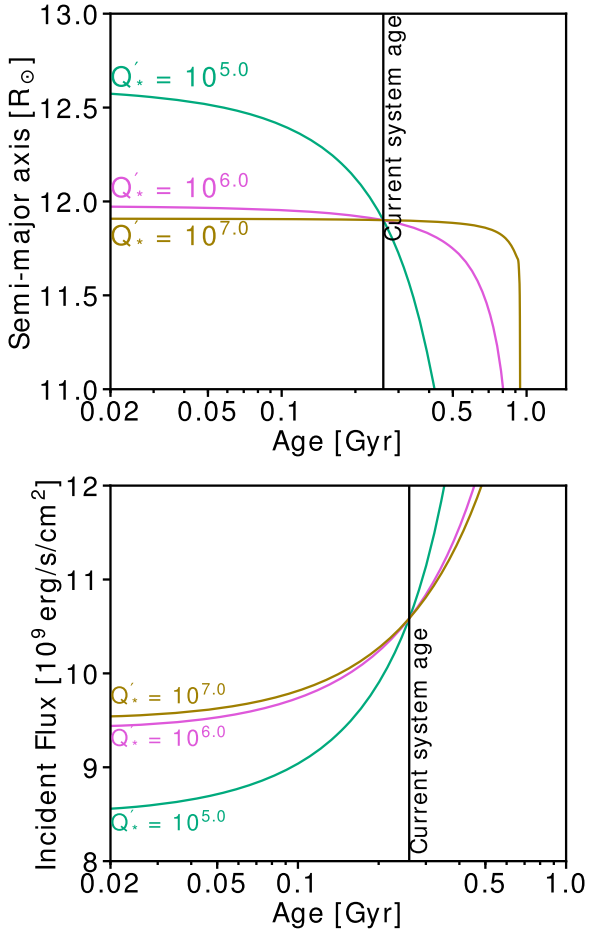

Figure 18. Evolution of the semimajor axis in units of stellar radius (top) and incident flux (stellar radiation) as a function of stellar age (bottom) of KELT-26 b for constant values of $Q_\star$ of 10^5 (turquoise), 10^6 (pink), and 10^7 (gold).

assuming that the spin period of the star has remained constant throughout its lifetime. Assuming that $Q_\star^{'}$ is constant, and as long as the orbital period has always remained longer than the stellar spin period, the assumption of a constant rotation does not affect the results. However, if that is not the case, the direction of the evolution would be reversed. Figures 17 and 18 show the semimajor and irradiation evolution of both systems.

8. Conclusion

In this paper, we presented the discovery of KELT-25 b, an ultrahot, substellar companion in a 4.4 day orbit around a young, rapidly rotating A star; and KELT-26 b, a puffy ultrahot Jupiter on a highly inclined, 3.3 day orbit around a young, slowly rotating Am star. Both systems were observed by the TESS mission. These companions both have exceptionally high equilibrium temperatures, and their host stars are bright, making them excellent candidates for follow-up observations. With a rotational velocity of $v \sin I_* = 114.2$ km s^{-1}, KELT-25 is among the most rapidly rotating A stars with transiting companions, while KELT-26 is, in contrast, among the slowest. The highly inflated radius of KELT-26 b can provide constraints on empirical mass–radius relations for giant planets. The orbital evolution of KELT-25 b suggests that the semimajor axis is increasing over time, a rather unusual trend for hot Jupiters, which could provide insights into migration mechanisms for these giant planets. With now roughly a dozen exoplanets detected around A stars, we begin to have a more comprehensive sample that enables a better understanding of the physical properties, formation, and evolution of these planetary systems.

The authors thank the anonymous referee for providing useful comments that improved the quality of this paper.

J.E.R. was supported by the Harvard Future Faculty Leaders Postdoctoral fellowship. Work by G.Z. is provided by NASA through Hubble Fellowship grant HST-HF2-51402.001-A awarded by the Space Telescope Science Institute, which is operated by the Association of Universities for Research in Astronomy, Inc., for NASA under contract NAS 5-26555. D.J.S. is supported by Penn State University's Eberly Research Fellowship. The Center for Exoplanets and Habitable Worlds is supported by the Pennsylvania State University, the Eberly College of Science, and the Pennsylvania Space Grant Consortium.

Support for this work was provided by NASA through Hubble Fellowship grant HST-HF2-51399.001 awarded to

J.K.T. by the Space Telescope Science Institute, which is operated by the Association of Universities for Research in Astronomy, Inc., for NASA under contract NAS5-26555.

M.N.G. acknowledges support from MIT's Kavli Institute as a Juan Carlos Torres Fellow.

C.Z. is supported by a Dunlap Fellowship at the Dunlap Institute for Astronomy & Astrophysics, funded through an endowment established by the Dunlap family and the University of Toronto. K.G.S. acknowledges support from the Vanderbilt Office of the Provost through the Vanderbilt Initiative in Data-intensive Astrophysics. T.N. and A.Y. are also grateful to Mizuki Isogai, Akira Arai, and Hideyo Kawakita for their technical support on observations at Koyama Astronomical Observatory. C.D.K. was supported by the Swarthmore College Provost's Office. J.L.-B. acknowledges support from FAPESP (grant 2017/23731-1). K.P. acknowledges support from NASA grants 80NSSC18K1009 and NNX17AB94G.

Funding for the TESS mission is provided by NASA's Science Mission directorate.

This research has made use of the Exoplanet Follow-up Observation Program website, which is operated by the California Institute of Technology under contract with the National Aeronautics and Space Administration under the Exoplanet Exploration Program.

Resources supporting this work were provided by the NASA High-End Computing (HEC) Program through the NASA Advanced Supercomputing (NAS) Division at Ames Research Center for the production of the SPOC data products.

This paper includes data collected by the TESS mission that are publicly available from the Mikulski Archive for Space Telescopes (MAST).

This work has made use of data from the European Space Agency (ESA) mission Gaia (https://www.cosmos.esa.int/gaia), processed by the Gaia Data Processing and Analysis Consortium (DPAC; https://www.cosmos.esa.int/web/gaia/dpac/consortium). Funding for the DPAC has been provided by national institutions, in particular the institutions participating in the Gaia Multilateral Agreement. This work makes use of observations from the LCO network. This research has made use of the NASA Exoplanet Archive, which is operated by the California Institute of Technology under contract with the National Aeronautics and Space Administration under the Exoplanet Exploration Program.

Based on observations obtained at the Gemini Observatory, which is operated by the Association of Universities for Research in Astronomy, Inc., under a cooperative agreement with the NSF on behalf of the Gemini partnership: the National Science Foundation (United States), National Research Council (Canada), CONICYT (Chile), Ministerio de Ciencia, Tecnología e Innovación Productiva (Argentina), Ministério da Ciência, Tecnologia e Inovação (Brazil), and Korea Astronomy and Space Science Institute (Republic of Korea). Some of the observations in the paper made use of the High-Resolution Imaging instrument Zorro at Gemini-South. Zorro was funded by the NASA Exoplanet Exploration Program and built at the NASA Ames Research Center by Steve B. Howell, Nic Scott, Elliott P. Horch, and Emmett Quigley.

This research made use of Lightkurve, a Python package for Kepler and TESS data analysis (Lightkurve Collaboration, 2018).

MINERVA-Australis is supported by Australian Research Council LIEF grant LE160100001, Discovery grant DP180100 972, the Mount Cuba Astronomical Foundation, and institutional partners the University of Southern Queensland, UNSW Australia, MIT, Nanjing University, George Mason University, the University of Louisville, the University of California Riverside, the University of Florida, and the University of Texas at Austin.

We respectfully acknowledge the traditional custodians of all lands throughout Australia and recognize their continued cultural and spiritual connection to the land, waterways, cosmos, and community. We pay our deepest respects to all elders, ancestors, and descendants of the Giabal, Jarowair, and Kambuwal nations, upon whose lands the MINERVA-Australis facility at Mt. Kent is situated. Resources supporting this work were provided by the NASA High-End Computing (HEC) Program through the NASA Advanced Supercomputing (NAS) Division at Ames Research Center for the production of the SPOC data products.

Facilities: FLWO 1.5 m (Tillinghast Reflector Echelle Spectrograph, TRES); Kilodegree Extremely Little Telescope (KELT); MINiature Exoplanet Radial Velocity Array (MINERVA); Las Cumbres Observatory at Tenerife (LCO TFN); University of Louisville Manner Telescope (ULMT, Mt. Lemmon); KeplerCam (FLWO 1.2 m); Stacja Obserwacji Tranzytów Egzoplanet w Suwałkach (SOTES); CROW Observatory; Koyama Astronomical Observatory (KAO); Gemini-South Zorro.

Software: EXOFASTv2 (Eastman et al. 2013; Eastman 2017), AstroImageJ (Collins et al. 2017), SPC (Buchhave et al. 2010).

ORCID iDs

Romy Rodríguez Martínez https://orcid.org/0000-0003-1445-9923
B. Scott Gaudi https://orcid.org/0000-0003-0395-9869
Joseph E. Rodriguez https://orcid.org/0000-0001-8812-0565
George Zhou https://orcid.org/0000-0002-4891-3517
Jonathan Labadie-Bartz https://orcid.org/0000-0002-2919-6786
Samuel N. Quinn https://orcid.org/0000-0002-8964-8377
Kaloyan Penev https://orcid.org/0000-0003-4464-1371
Thiam-Guan Tan https://orcid.org/0000-0001-5603-6895
David W. Latham https://orcid.org/0000-0001-9911-7388
John F. Kielkopf https://orcid.org/0000-0003-0497-2651
Brett Addison https://orcid.org/0000-0003-3216-0626
Steve B. Howell https://orcid.org/0000-0002-2532-2853
David Ciardi https://orcid.org/0000-0002-5741-3047
Carl Ziegler https://orcid.org/0000-0002-0619-7639
Keivan G. Stassun https://orcid.org/0000-0002-3481-9052
Marshall C. Johnson https://orcid.org/0000-0002-5099-8185
Jason D. Eastman https://orcid.org/0000-0003-3773-5142
Robert J. Siverd https://orcid.org/0000-0001-5016-3359
Thomas G. Beatty https://orcid.org/0000-0002-9539-4203
Luke Bouma https://orcid.org/0000-0002-0514-5538
Timothy Bedding https://orcid.org/0000-0001-5222-4661
Joshua Pepper https://orcid.org/0000-0002-3827-8417
Joshua Winn https://orcid.org/0000-0002-4265-047X
Michael B. Lund https://orcid.org/0000-0003-2527-1598
Steven Villanueva, Jr. https://orcid.org/0000-0001-6213-8804
Daniel J. Stevens https://orcid.org/0000-0002-5951-8328
Eric L. N. Jensen https://orcid.org/0000-0002-4625-7333
Jeffrey D. Crane https://orcid.org/0000-0002-5226-787X
Andrei Tokovinin https://orcid.org/0000-0002-2084-0782

Mark E. Everett https://orcid.org/0000-0002-0885-7215
C. G. Tinney https://orcid.org/0000-0002-7595-0970
Michael Fausnaugh https://orcid.org/0000-0002-9113-7162
Daniel Bayliss https://orcid.org/0000-0001-6023-1335
Allyson Bieryla https://orcid.org/0000-0001-6637-5401
Phillip A. Cargile https://orcid.org/0000-0002-1617-8917
Karen A. Collins https://orcid.org/0000-0001-6588-9574
Knicole D. Colón https://orcid.org/0000-0001-8020-7121
Phil Evans https://orcid.org/0000-0002-8465-3353
Dax L. Feliz https://orcid.org/0000-0002-2457-7889
Rudolf B. Kuhn https://orcid.org/0000-0002-4236-9020
Mark Manner https://orcid.org/0000-0002-9411-7271
Somayeh Khakpash https://orcid.org/0000-0002-1910-7065
Jennifer L. Marshall https://orcid.org/0000-0003-0710-9474
Kim K. McLeod https://orcid.org/0000-0001-9504-1486
Matthew T. Penny https://orcid.org/0000-0001-7506-5640
Phillip A. Reed https://orcid.org/0000-0002-5005-1215
Chris Stockdale https://orcid.org/0000-0003-2163-1437
Xinyu Yao https://orcid.org/0000-0003-4554-5592
Roland Vanderspek https://orcid.org/0000-0001-6763-6562
Jon M. Jenkins https://orcid.org/0000-0002-4715-9460
Wei-Chun Jao https://orcid.org/0000-0003-0193-2187
Paul Butler https://orcid.org/0000-0003-1305-3761
Robert Wittenmyer https://orcid.org/0000-0001-9957-9304
Brendan P. Bowler https://orcid.org/0000-0003-2649-2288
Jonathan Horner https://orcid.org/0000-0002-1160-7970
Stephen R. Kane https://orcid.org/0000-0002-7084-0529
Timothy D. Morton https://orcid.org/0000-0002-8537-5711
Peter Plavchan https://orcid.org/0000-0002-8864-1667
Hui Zhang https://orcid.org/0000-0003-3491-6394
Nicholas J. Scott https://orcid.org/0000-0003-1038-9702
Rachel A. Matson https://orcid.org/0000-0001-7233-7508
Andrew W. Mann https://orcid.org/0000-0003-3654-1602
Diana Dragomir https://orcid.org/0000-0003-2313-467X
Max Günther https://orcid.org/0000-0002-3164-9086
Eric B. Ting https://orcid.org/0000-0002-8219-9505
Ana Glidden https://orcid.org/0000-0002-5322-2315

References

Addison, B., Wright, D. J., Wittenmyer, R. A., et al. 2019, PASP, 131, 115003
Alard, C. 2000, A&AS, 144, 363
Alard, C., & Lupton, R. H. 1998, ApJ, 503, 325
Alonso, R., Brown, T. M., Charbonneau, D., et al. 2007, in ASP Conf. Ser. 366, Transiting Extrapolar Planets Workshop, ed. C. Afonso, D. Weldrake, & T. Henning (San Francisco, CA: ASP), 13
Alsubai, K. A., Parley, N. R., Bramich, D. M., et al. 2011, MNRAS, 417, 709
Anderson, D. R., Temple, L. Y., Nielsen, L. D., et al. 2018, arXiv:1809.04897
Bakos, G. Á, Csubry, Z., Penev, K., et al. 2013, PASP, 125, 154
Bakos, G. Á, Kovács, G., Torres, G., et al. 2007, ApJ, 670, 826
Barclay, T., Pepper, J., & Quintana, E. V. 2018, ApJS, 239, 2
Barentsen, G., Hedges, C. L., De Mirand a Cardoso, J. V., et al. 2019, KeplerGO/lightkurve: Lightkurve v1.0b29, Zenodo, doi:10.5281/zenodo.2565212
Barnes, J. W. 2009, ApJ, 705, 683
Bayliss, D., Gillen, E., Eigmüller, P., et al. 2018, MNRAS, 475, 4467
Bell, T. J., & Cowan, N. B. 2018, ApJL, 857, L20
Bensby, T., Feltzing, S., & Lundström, I. 2003, A&A, 410, 527
Berta, Z. K., Irwin, J., Charbonneau, D., Burke, C. J., & Falco, E. E. 2012, AJ, 144, 145
Bieryla, A., Collins, K., Beatty, T. G., et al. 2015, AJ, 150, 12
Blake, C. H., Latham, D. W., & Bloom, J. S. 2007, in ASP Conf. Ser. 366, The PAIRITEL Ultracool Dwarf Transit Survey, ed. C. Afonso, D. Weldrake, & T. Henning (San Francisco, CA: ASP), 87
Borucki, W. J., Koch, D., Basri, G., et al. 2010, Sci, 327, 977
Bovy, J. 2017, MNRAS, 470, 1360
Brahm, R., Espinoza, N., Jordán, A., et al. 2019, AJ, 158, 45
Buchhave, L. A., Bakos, G. Á, Hartman, J. D., et al. 2010, ApJ, 720, 1118
Buchhave, L. A., Latham, D. W., Johansen, A., et al. 2012, Natur, 486, 375
Carmichael, T. W., Quinn, S. N., Mustill, A. e. J., et al. 2020, AJ, 160, 53
Castelli, F., & Kurucz, R. L. 2003, in IAU Symp. 210, Modeling of Stellar Atmospheres, ed. N. Piskunov, W. W. Weiss, & D. F. Gray (San Fransisco, CA: ASP), A20
Cauley, P. W., Shkolnik, E. L., Ilyin, I., et al. 2019, AJ, 157, 69
Charbonneau, D., Berta, Z. K., Irwin, J., et al. 2009, Natur, 462, 891
Charbonneau, D., Brown, T. M., Latham, D. W., & Mayor, M. 2000, ApJL, 529, L45
Choi, J., Dotter, A., Conroy, C., et al. 2016, ApJ, 823, 102
Ciardi, D. R., Beichman, C. A., Horch, E. P., & Howell, S. B. 2015, ApJ, 805, 16
Collier Cameron, A., Guenther, E., Smalley, B., et al. 2010, MNRAS, 407, 507
Collier Cameron, A., Pollacco, D., Hellier, C., et al. 2009, in IAU Symp. 253, Transiting Planets, ed. F. Pont, D. Sasselov, & M. J. Holman (Cambridge: Cambridge Univ. Press), 29
Collier Cameron, A., Wilson, D. M., West, R. G., et al. 2007, MNRAS, 380, 1230
Collins, K. A., Collins, K. I., Pepper, J., et al. 2018, AJ, 156, 234
Collins, K. A., Kielkopf, J. F., Stassun, K. G., & Hessman, F. V. 2017, AJ, 153, 77
Coşkunoğlu, B., Ak, S., Bilir, S., et al. 2011, MNRAS, 412, 1237
Crane, J. D., Shectman, S. A., Butler, R. P., et al. 2010, Proc. SPIE, 7735, 773553
Cutri, R. M., Skrutskie, M. F., van Dyk, S., et al. 2003, yCat, 2246, 0
Dawson, R. I., & Johnson, J. A. 2018, ARA&A, 56, 175
Dawson, R. I., Murray-Clay, R. A., & Johnson, J. A. 2015, ApJ, 798, 66
Delrez, L., Gillon, M., Queloz, D., et al. 2018, Proc. SPIE, 10700, 107001I
Demory, B.-O., & Seager, S. 2011, ApJS, 197, 12
Dholakia, S., Dholakia, S., Cody, A. M., et al. 2019, PASP, 131, 114402
Donati, J.-F., Semel, M., Carter, B. D., Rees, D. E., & Collier Cameron, A. 1997, MNRAS, 291, 658
Dorval, P., Talens, G. J. J., Otten, G. P. P. L., et al. 2020, A&A, 635, A60
Dotter, A. 2016, ApJS, 222, 8
Drake, A. J. 2003, ApJ, 589, 1020
Eastman, J. 2017, EXOFASTv2: Generalized Publication-Quality Exoplanet Modeling Code, Astrophysics Source Code Library, ascl:1710.003
Eastman, J., Gaudi, B. S., & Agol, E. 2013, PASP, 125, 83
Eastman, J. D., Rodriguez, J. E., Agol, E., et al. 2019, arXiv:1907.09480
Esteves, L. J., De Mooij, E. J. W., & Jayawardhana, R. 2015, ApJ, 804, 150
Fűrész, G. 2008, PhD thesis, Univ. of Szeged
Gaia Collaboration, Brown, A. G. A., Vallenari, A., et al. 2018, A&A, 616, A1
Gaudi, B. S., Stassun, K. G., Collins, K. A., et al. 2017, Natur, 546, 514
Gaudi, B. S., & Winn, J. N. 2007, ApJ, 655, 550
Gillon, M., Triaud, A. H. M. J., Demory, B.-O., et al. 2017, Natur, 542, 456
Gould, A., & Morgan, C. W. 2003, ApJ, 585, 1056
Gould, A., Pepper, J., & DePoy, D. L. 2003, ApJ, 594, 533
Gravity Collaboration, Abuter, R., Amorim, A., et al. 2019, A&A, 625, L10
Grether, D., & Lineweaver, C. H. 2006, ApJ, 640, 1051
Hartman, J. D., Bakos, G. Á, Buchhave, L. A., et al. 2015, AJ, 150, 197
Hatzes, A. P., Endl, M., Cochran, W. D., et al. 2018, AJ, 155, 120
Hébrard, G., Désert, J. M., Díaz, R. F., et al. 2010, A&A, 516, A95
Hellier, C., Anderson, D. R., Bouchy, F., et al. 2019, MNRAS, 482, 1379
Henry, G. W., Marcy, G. W., Butler, R. P., & Vogt, S. S. 2000, ApJL, 529, L41
Hoeijmakers, H. J., Ehrenreich, D., Kitzmann, D., et al. 2019, A&A, 627, A165
Høg, E., Fabricius, C., Makarov, V. V., et al. 2000, A&A, 355, L27
Howell, S. B., Everett, M. E., Sherry, W., Horch, E., & Ciardi, D. R. 2011, AJ, 142, 19
Howell, S. B., Scott, N. J., Matson, R. A., Horch, E. P., & Stephens, A. 2019, AJ, 158, 113
Jenkins, J. M., Twicken, J. D., McCauliff, S., et al. 2016, Proc. SPIE, 9913, 99133E
Johnson, J. A., Clanton, C., Howard, A. W., et al. 2011, ApJS, 197, 26
Johnson, J. A., Fischer, D. A., Marcy, G. W., et al. 2007, ApJ, 665, 785
Johnson, M. C., Cochran, W. D., Albrecht, S., et al. 2014, ApJ, 790, 30
Johnson, M. C., Cochran, W. D., Collier Cameron, A., & Bayliss, D. 2015, ApJL, 810, L23
Johnson, M. C., Rodriguez, J. E., Zhou, G., et al. 2018, AJ, 155, 100
Kitzmann, D., Heng, K., Rimmer, P. B., et al. 2018, ApJ, 863, 183
Kounkel, M., & Covey, K. 2019, AJ, 158, 122
Kovács, G., Zucker, S., & Mazeh, T. 2002, A&A, 391, 369
Kraft, R. P. 1967, ApJ, 150, 551
Kuhn, R. B., Rodriguez, J. E., Collins, K. A., et al. 2016, MNRAS, 459, 4281
Lesage, A. L., Spronck, J. F. P., Stuik, R., et al. 2014, Proc. SPIE, 9145, 914514

Lightkurve Collaboration, Cardoso, J. V. D. M., Hedges, C., et al. 2018, Lightkurve: Kepler and TESS Time Series Analysis in Python, v1.11, Astrophysics Source Code Library, ascl:1812.013
Loeb, A., & Gaudi, B. S. 2003, ApJL, 588, L117
Lomb, N. R. 1976, Ap&SS, 39, 447
Lothringer, J. D., Barman, T., & Koskinen, T. 2018, ApJ, 866, 27
Lund, M. B., Rodriguez, J. E., Zhou, G., et al. 2017, AJ, 154, 194
Matson, R. A., Howell, S. B., & Ciardi, D. 2019, AJ, 157, 211
McCullough, P. R., Stys, J. E., Valenti, J. A., et al. 2005, PASP, 117, 783
McInnes, L., Healy, J., & Astels, S. 2017, JOSS, 2, 205
Murphy, S. J., Hey, D., Van Reeth, T., & Bedding, T. R. 2019, MNRAS, 485, 2380
Nielsen, L. D., Bouchy, F., Turner, O., et al. 2019, A&A, 623, A100
Nutzman, P., & Charbonneau, D. 2008, PASP, 120, 317
Pavlenko, Y. V., Jenkins, J. S., Jones, H. R. A., Ivanyuk, O., & Pinfield, D. J. 2012, MNRAS, 422, 542
Paxton, B., Bildsten, L., Dotter, A., et al. 2011, ApJS, 192, 3
Paxton, B., Cantiello, M., Arras, P., et al. 2013, ApJS, 208, 4
Paxton, B., Marchant, P., Schwab, J., et al. 2015, ApJS, 220, 15
Penev, K., Zhang, M., & Jackson, B. 2014, PASP, 126, 553
Pepper, J., Kuhn, R. B., Siverd, R., James, D., & Stassun, K. 2012, PASP, 124, 230
Pepper, J., Pogge, R. W., DePoy, D. L., et al. 2007, PASP, 119, 923
Pepper, J., Siverd, R. J., Beatty, T. G., et al. 2013, ApJ, 773, 64
Pollacco, D. L., Skillen, I., Collier Cameron, A., et al. 2006, PASP, 118, 1407
Quinn, S. N., White, R. J., Latham, D. W., et al. 2012, ApJL, 756, L33
Ricker, G. R., Winn, J. N., Vanderspek, R., et al. 2015, JATIS, 1, 014003
Rodriguez, J. E., Eastman, J. D., Zhou, G., et al. 2019a, AJ, 158, 197
Rodriguez, J. E., Quinn, S. N., Huang, C. X., et al. 2019b, AJ, 157, 191
Royer, F., Zorec, J., & Gómez, A. E. 2007, A&A, 463, 671
Scargle, J. D. 1982, ApJ, 263, 835
Schlaufman, K. C. 2010, ApJ, 719, 602
Schlegel, D. J., Finkbeiner, D. P., & Davis, M. 1998, ApJ, 500, 525
Scott, N. J., & Howell, S. B. 2018, Proc. SPIE, 10701, 107010G
Siverd, R. J., Beatty, T. G., Pepper, J., et al. 2012, ApJ, 761, 123
Siverd, R. J., Collins, K. A., Zhou, G., et al. 2018, AJ, 155, 35
Stassun, K. G., Oelkers, R. J., Paegert, M., et al. 2019, AJ, 158, 138
Stassun, K. G., & Torres, G. 2018, ApJ, 862, 61
Stephan, A. P., Naoz, S., & Gaudi, B. S. 2018, AJ, 156, 128
Stephan, A. P., Naoz, S., Gaudi, B. S., & Salas, J. M. 2020, ApJ, 889, 45
Šubjak, J., Sharma, R., Carmichael, T. W., et al. 2020, AJ, 159, 151
Talens, G. J. J., Albrecht, S., Spronck, J. F. P., et al. 2017, A&A, 606, A73
Talens, G. J. J., Justesen, A. B., Albrecht, S., et al. 2018, A&A, 612, A57
Tokovinin, A. 2018, PASP, 130, 035002
Tokovinin, A., Fischer, D. A., Bonati, M., et al. 2013, PASP, 125, 1336
Triaud, A. H. M. J. 2018, in Handbook of Exoplanets, ed. H. Deeg & J. Belmonte (Cham: Springer), 2
Winn, J. N. 2010, in Exoplanets, ed. S. Seager (Tucson, AZ: Univ. Arizona Press), 55
Wong, I., Shporer, A., Morris, B. M., et al. 2020, AJ, 160, 88
Zacharias, N., Finch, C., & Frouard, J. 2017, yCat, 1340, 0
Zacharias, N., Finch, C. T., Girard, T. M., et al. 2013, AJ, 145, 44
Zhou, G., Bakos, G. Á, Bayliss, D., et al. 2019a, AJ, 157, 31
Zhou, G., Huang, C. X., Bakos, G. Á, et al. 2019b, AJ, 158, 141
Zhou, G., Rodriguez, J. E., Collins, K. A., et al. 2016, AJ, 152, 136
Ziegler, C., Tokovinin, A., Briceno, C., et al. 2020, AJ, 159, 19
Zorec, J., & Royer, F. 2012, A&A, 537, A120